TSL/ISV-95-0120
PAR-LPTHE-95-29
May 1995, revised February 1996

ISSN 0284-2769

Charm Production and High Energy Atmospheric Muon and Neutrino Fluxes

M. Thunman[1], G. Ingelman[2]

Department of Radiation Sciences, Uppsala University, Box 535, S-751 21 Uppsala, Sweden

P. Gondolo[3]

Physique Théorique et Hautes Energies, Université de Paris 7, Boite 7109, 2 place Jussieu, F-75251 Paris, France

Abstract: Production of muons and neutrinos in cosmic ray interactions with the atmosphere has been investigated with Monte Carlo models for hadronic interactions. The resulting conventional muon and neutrino fluxes (from π and K decays) agree well with earlier calculations, whereas our prompt fluxes from charm decays are significantly lower than earlier estimates. Charm production is mainly considered as a well defined perturbative QCD process, but we also investigate a hypothetical non-perturbative intrinsic charm component in the proton. The lower charm rate implies better prospects for detecting very high energy neutrinos from cosmic sources.

1 Introduction

The flux of muons and neutrinos at the earth has an important contribution from decays of particles produced through the interaction of cosmic rays in the atmosphere (for a recent introduction see [1]). This has an interest in its own right, since it reflects primary interactions at energies that can by far exceed the highest available accelerator energies. It is also a background in studies of neutrinos from cosmic sources as attempted in large neutrino telescopes, such as AMANDA [2], BAIKAL [3], DUMAND [4] and NESTOR [5].

Here we present a detailed study of muon and neutrino production in cosmic ray interactions with nuclei in the atmosphere using Monte Carlo simulations [6].

At GeV energies the atmospheric muon and neutrino fluxes are dominated by 'conventional' sources, *i.e.* decays of relatively long-lived particles such as π and K mesons. This is well understood from earlier studies [7, 8, 9], with which our investigations agree. With increasing energy, the probability increases that such particles interact in the atmosphere before decaying. This implies that even a small fraction of short-lived particles can give the dominant contribution to high energy muon and neutrino fluxes. These 'prompt' muons and neutrinos arise through semi-leptonic decays of hadrons containing heavy quarks, most notably charm.

Available data in the multi-TeV energy range, obtained with surface and underground detectors (see *e.g.* refs. [10–13]), are still too discrepant to draw definitive conclusions on the flux of

[1] thunman@tsl.uu.se
[2] ingelman@tsl.uu.se, also at DESY, Hamburg.
[3] Present address: Oxford University, Dept. of Physics, 1 Keble Road, OX1 3NP, UK, p.gondolo1@physics.oxford.ac.uk

prompt muons and neutrinos from charm. Furthermore, estimates of these prompt fluxes [7,14–21] vary by a few orders of magnitude due to the different models used to calculate the charm hadron cross section and energy spectra. This huge model dependence is due to the need of extrapolating charm production data obtained at accelerator energies to the orders-of-magnitude higher energies of the relevant cosmic ray collisions. Obviously, this extrapolation can only be trustworthy if starting from proper charm production data and using a sound physical model. The main contribution of our study is in this context. First, we use recent charm production cross section measurements that form a consistent set of data, but disagree with some of the early measurements that were substantially higher. Secondly, we apply state-of-the-art models to simulate charm particle production through perturbative QCD processes in high energy hadron-hadron interactions. In addition, we investigate a possible non-perturbative mechanism using the hypothesis of an intrinsic charm quark component in the nucleon.

In the following we first (section 2) discuss the generalities of cosmic ray interactions in the atmosphere resulting in a set of transport or cascade equations for particle propagation. These equations are then solved by two different methods: a direct Monte Carlo simulation of the cascade interactions (section 3) and a semi-analytic method (section 4) giving consistent results for the conventional and prompt muon and neutrino fluxes. Section 5 gives an account of the Monte Carlo model used to obtain the energy spectra of secondaries in the basic hadron-hadron interaction, in particular concerning charm production in perturbative QCD. In section 6 we investigate consequences of the non-standard hypothesis of a non-perturbative intrinsic charm quark component in the nucleon. We then (section 7) compare our results with previous model calculations and discuss differences in terms of the different charm production models. We conclude (section 8) by some remarks and by putting our results in a general context of various astrophysical sources of high energy neutrinos.

2 Cosmic ray interactions in the atmosphere

2.1 The spectrum of cosmic rays

Fluxes of secondary particles (hadrons and leptons) originate from nucleon–nucleon encounters, even when the nucleons are bound in nuclei, because nuclear binding energies are much lower than the energies of interest in this study (100 GeV – 10^9 GeV). So the relevant quantity to consider is the flux of nucleons. Following [1, 9, 17] we have assumed a power law primary nucleon flux

$$\phi_N(E)\ \left[\frac{\text{nucleons}}{\text{cm}^2\,\text{s}\,\text{sr}\,\text{GeV}/A}\right] = \begin{cases} 1.7\,E^{-2.7} & \text{for } E < 5\cdot 10^6\,\text{GeV} \\ \\ 174\,E^{-3} & \text{for } E > 5\cdot 10^6\,\text{GeV}. \end{cases} \tag{1}$$

The normalisation constant 1.7 is derived [22] from the directly measured primary spectrum using balloon-borne emulsion chambers in JACEE [23]. To within some 10% this agrees with more indirectly derived spectra based on measured atmospheric muon fluxes [24], and is also compatible with the data discussed in ref. [25]. The cosmic ray composition is dominated by protons with only a smaller component of neutrons in nuclei [22, 25]. Only primary protons are considered here, since in this study we are interested in quantities that are essentially independent of the cosmic ray composition. At the energies of interest ($E \gtrsim 100$ GeV), the cosmic ray flux can be considered isotropic (the anisotropy being $\lesssim 5\%$ [26]).

2.2 The model for the atmosphere

In studying the propagation of particles through the atmosphere, an important quantity is the amount of atmosphere X, in g/cm^2, traversed by the particle. This so-called slant depth is the integral of the atmospheric density from the top of the atmosphere downward along the trajectory of the incident particle. At distance ℓ from the ground along a direction at an angle θ from the zenith, the slant depth is defined as

$$X(\ell,\theta) = \int_\ell^\infty \rho[h(l,\theta)]dl, \tag{2}$$

where $\rho[h(l,\theta)]$ is the atmospheric density at the altitude $h(l,\theta)$,

$$h(l,\theta) = \sqrt{R_\oplus^2 + 2lR_\oplus\cos\theta + l^2} - R_\oplus \;\approx\; l\cos\theta \;+\; \frac{l^2}{2\,R_\oplus}\,\sin^2\theta. \tag{3}$$

Here $R_\oplus$ is the radius of the Earth and the approximate equality applies for zenith angles not too far from vertical, $\theta \lesssim 60°$.

The atmospheric density is not a simple function of height, even neglecting local atmospheric turbulence. The temperature, which is related to the density through the equation of state, decreases with increasing height until the tropopause (8–17 km), stays almost constant in the lower stratosphere (-56.42°C up to 20–30 km), then increases until the stratopause (50 km) before decreasing again at the highest altitudes ($>$ 50 km). However, since most particle interactions occur at heights between 10 and 40 km (demonstrated in Fig. 1 below), we need only a simple model for the density profile of the stratosphere. We therefore adopt an isothermal model,

$$\rho(h) = \rho_0 e^{-h/h_0}, \tag{4}$$

with scale height $h_0 = 6.4$ km and $X_0 = \rho_0 h_0 = 1300\,\mathrm{g/cm^2}$, values which adequately describe the density of the stratosphere ($< 2\%$ error in the vertical depth between 10 and 30 km and $< 16\%$ between 30 and 40 km).

Concerning the atmospheric composition, a good approximation, valid up to a height of 100 km, is 78.4% nitrogen, 21.1% oxygen and 0.5% argon (obtained from data in [27]). This leads to an average atomic number of $\langle A\rangle = 14.5$.

2.3 Particle interactions with air nuclei

To obtain the flux of atmospheric muons and neutrinos one needs to consider the particle production mechanisms in strong interaction dynamics. The cosmic ray particles, represented by protons (see section 2.1), interact with nuclei in the atmosphere to produce secondary particles. These proton-nucleus collisions can, for our purposes, be well represented by the simpler proton-nucleon collisions and a rescaling of the cross section

$$\sigma(pA) = A^\alpha \sigma(pN) \tag{5}$$

using a power dependence on the number A of nucleons in the target nucleus. For inclusive cross sections, with $\sigma(pN)$ of order 10 mb, the interaction occurs with nucleons at the surface resulting in $\alpha \simeq 2/3$ as verified experimentally.

The inelastic pN interaction produces secondary hadrons with a multiplicity increasing essentially logarithmically with the cms energy ($s_{pN} = 2m_N c^2 E_p$). The formation time of a hadron is the normal strong interaction time scale. In the particles rest system this corresponds to a formation length of ~ 1 fm, which is Lorentz transformed with a γ-factor to the target nucleus

rest frame and thus becomes proportional to the energy of the particle [28]. Therefore, fast particles have formation lengths that exceed the size of the nucleus whereas only slow particles are formed and can re-interact within the target nucleus. Therefore, intra-nuclear cascade effects are not important for the energetic particle production studied here.

Of importance for our considerations are the energy distributions of secondary hadrons produced in the collisions

$$\frac{\mathrm{d}n(kA \to hY; E_k, E_h)}{\mathrm{d}E_h} = \frac{1}{\sigma_{kA}(E_k)} \frac{\mathrm{d}\sigma(kA \to hY; E_k, E_h)}{\mathrm{d}E_h}, \tag{6}$$

where $\mathrm{d}n(kA \to hY; E_k, E_h)$ is the number of hadrons h with energies between E_h and $E_h + \mathrm{d}E_h$ produced in the collision of the incoming particle k with an air nucleus of atomic number A, and σ_{kA} is the total inelastic cross section for particle k – nucleus A collisions. Experiments studying proton–nucleus [29] and heavy ion [30] collisions obtain energy spectra that are approximately the same as in proton–proton collisions, confirming that the interactions are essentially proton–nucleon. So we adopt an energy distribution $\mathrm{d}n_{kh}/\mathrm{d}E_h$ independent of the atomic number of the target.

The energy spectra in Eq. (6) can also be expressed as

$$\frac{\mathrm{d}n_{kh}}{\mathrm{d}x_F} = \frac{1}{\sigma_{kA}} \frac{\mathrm{d}\sigma(kA \to hY)}{\mathrm{d}x_F} \tag{7}$$

in terms of the scaled longitudinal momentum or Feynman-x variable $x_F = p_z/p_{z,max}$ ($\approx E_h/E_k$ at large energies) where the z-axis is along the incoming particle momentum. If these distributions are independent of the cms energy (*i.e.* incoming particle energy E_k), then 'Feynman scaling' holds. The validity or breaking of this scaling in different models for particle production is an important issue as will be demonstrated later.

To obtain the energy spectra of the particles produced in proton-nucleon collisions we use the Lund Monte Carlo simulation programs PYTHIA and JETSET [31]. These have proven very successful in describing the multi-particle final state in various kinds of interactions, including hadron-hadron collisions. An advantage with this Monte Carlo approach is the access to the complete final state as well as a proper account of the decay of unstable particles. Conventional muons and neutrinos are obtained from an inclusive event sample generated with PYTHIA in a mode simulating minimum bias proton-proton interactions (including diffractive scattering). The particle production results from Lund model [32] hadronization of colour string fields between partons scattered in semi-soft QCD interactions. The prompt muons and neutrinos, on the other hand, are obtained from a dedicated charm production simulation using PYTHIA. Here, charm particles arise from the hadronization of charm quarks produced in the processes $gg \to c\bar{c}$ and $q\bar{q} \to c\bar{c}$ as calculated with leading order perturbative QCD matrix elements. A more detailed account of the Monte Carlo model is given in section 5. Since non-perturbative charm production is neither well established nor well defined, it is not part of our main Monte Carlo study but investigated separately based on the intrinsic charm hypothesis in section 6.

2.4 Particle propagation in the atmosphere

Propagation of high energy particles through the atmosphere may be described by a set of transport or cascade equations. In principle, the transport equations for nucleons, mesons, unstable baryons and leptons are coupled, but under the reasonable assumptions made below they can be greatly simplified.

Nucleons constitute the initial primary flux. We consider nucleon absorption and regeneration in nucleon–air inelastic collisions, but neglect the certainly small contribution to the nucleon

flux from the interaction of unstable hadrons with air nuclei. Absorption is described by the interaction thickness λ_N of nucleons N in air, *i.e.* the average amount of atmosphere (in g/cm^2) traversed between successive collisions with air nuclei. It is given by

$$\lambda_N(E) = \frac{\rho(h)}{\sum_A \sigma_{NA}(E)\, n_A(h)}, \tag{8}$$

where $n_A(h)$ is the number density of air nuclei of atomic number A at height h and $\sigma_{NA}(E)$ is the inclusive inelastic cross section for collisions of nucleons with nuclei A. Note that to a good approximation $\lambda_N(E)$ does not depend on the height h because the atmospheric composition is approximately independent of the height up to 100 km.

Nucleon fluxes develop according to the cascade equation

$$\frac{\mathrm{d}\phi_N}{\mathrm{d}X} = -\frac{\phi_N}{\lambda_N} + S(NA \to NY). \tag{9}$$

Here $\phi_N(E, X, \theta)$ is the nucleon flux at slant depth X in the atmosphere at zenith angle θ, $\lambda_N(E)$ has been defined in Eq. (8), and $S(NA \to NY)$ is the nucleon–nucleon regeneration function in air

$$S(NA \to NY) = \int_E^\infty \mathrm{d}E' \, \frac{\phi_N(E')}{\lambda_N(E')} \, \frac{\mathrm{d}n(NA \to NY; E', E)}{\mathrm{d}E}. \tag{10}$$

Mesons and unstable baryons, in addition to interact with the atmosphere, can also decay. The decay length $d(E)$, *i.e.* the distance traveled in a mean decay time, is simply

$$d(E) = c\,\beta\,\gamma\,\tau, \tag{11}$$

where τ is the particle proper lifetime, $\gamma = E/mc^2$ is its Lorentz factor, m its mass, and β its speed in units of the speed of light c. The decay length increases with particle energy because of relativistic time dilation; faster particles can travel longer before decaying. This implies an increased probability to interact before decaying. It is exactly because of this energy-dependent competition between decay and interaction that the muon and neutrino fluxes from charm mesons overcome those from pions and kaons at high enough energy.

We assume that mesons and unstable baryons (collectively unstable hadrons) are generated in nucleon–air collisions and regenerated in hadron–air collisions, but neglect generation of unstable hadrons of other types in collisions of hadrons against air nuclei. This approximation is reasonable since the fluxes of unstable hadrons are at least a factor of ~ 10 smaller than the fluxes of nucleons. Thus for mesons and unstable baryons we have

$$\frac{\mathrm{d}\phi_M}{\mathrm{d}X} = S(NA \to MY) - \frac{\phi_M}{\rho d_M} - \frac{\phi_M}{\lambda_M} + S(MA \to MY), \tag{12}$$

where $\lambda_M(E)$ is the hadron interaction thickness in air (analogous to Eq. (8)), and $S(NA \to MY)$ and $S(MA \to MY)$ are defined analogously to Eq. (10).

Finally we consider muons, muon-neutrinos and electron-neutrinos. At the energies we are interested in, energy loss, absorption and muon decay can be neglected and the transport equation for lepton $\ell = \mu^\pm$, ν_μ, $\bar{\nu}_\mu$, ν_e, $\bar{\nu}_e$ contains only source terms

$$\frac{\mathrm{d}\phi_\ell}{\mathrm{d}X} = \sum_M S(M \to \ell Y), \tag{13}$$

where the sum runs over all mesons and unstable baryons decaying into muons and neutrinos $M = \pi^{\pm}$, $K^{\pm}$, K^0, $D^{\pm}$, D^0, $\bar{D}^0$, $D_s^{\pm}$, $\Lambda_c^{\pm}$. $S(M \to \ell Y)$ describes lepton production in hadron decays,

$$S(M \to \ell Y) = \int_E^{\infty} \mathrm{d}E_M \, \frac{\phi_M(E_M)}{\rho d_M(E_M)} \, \frac{\mathrm{d}n(M \to \ell Y; E_M, E)}{\mathrm{d}E}, \tag{14}$$

where $\mathrm{d}n(M \to \ell Y; E_M, E)$ is the number of leptons with energy between E and $E + \mathrm{d}E$ produced in the decay of hadron M.

Muons and neutrinos born out of pions and kaons are traditionally called 'conventional,' while those born out of charmed hadrons are called 'prompt.' This originates from the fact that up to $\sim 10^7$ GeV very short-lived charmed particles have negligible probability of being absorbed in the atmosphere before decaying. Up to $\sim 10^7$ GeV the prompt flux is therefore essentially independent of the zenith angle. The conventional muon and neutrino fluxes are instead lower in the vertical direction, where the amount of atmosphere traversed in a given meson decay length is larger. The prompt flux is therefore relatively more important in the vertical direction, and we will predominantly consider this direction.

3 Simulation of cascade interactions

One way of solving the transport equations described in the previous section is to simulate the particle cascade with a Monte Carlo program. Here we describe our simulation algorithm.

A cosmic ray proton is generated. Its energy is drawn from a flat distribution in $\log E$, and a weight is assigned to it in order to reproduce the shape of the primary spectrum.

An interaction height h for the cosmic ray proton is then chosen in the following way. Primary nucleons propagate down through the atmosphere according to Eq. (9) without the regeneration term $S(NA \to NY)$. From the solution to this equation, $\phi(h) = \phi_\infty \exp(-X(h)/\lambda_N)$, the probability distribution for the primary interaction height can be obtained. Using a standard Monte Carlo technique, we generate this distribution by replacing $\phi(h)/\phi_\infty$ with a uniform

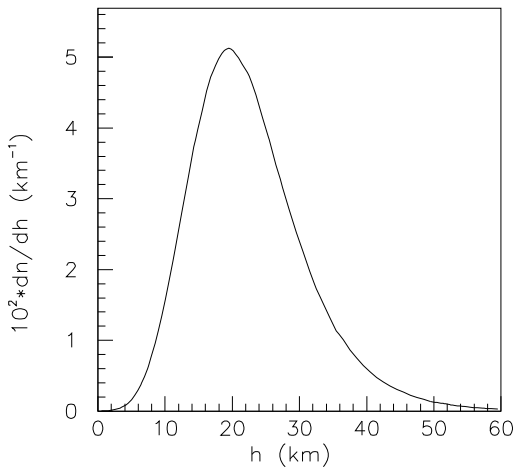

Figure 1: *Distribution of the altitude for the primary interactions as obtained in the cascade simulations.*

random number $R \in]0,1[$ and then solving for the interaction height h. This can be done analytically for the isothermal atmospheric model in Eq. (4) in the vertical direction, for which we obtain

$$h = -h_0 \ln\left(\frac{-\lambda_N \ln R}{X_0}\right) . \tag{15}$$

Fig. 1 shows the height distribution so obtained (neglecting the logarithmic energy dependence of λ_N), which confirms that, under the assumptions made, most particle interactions occur at heights between 10 and 40 km.

A proton-nucleon interaction is then generated in full detail with PYTHIA [31] resulting in a complete final state of particles. Secondary particles are followed through the atmosphere where they decay or interact producing cascades. Secondary nucleons give a flux that is rather small compared to the primary flux and could therefore be neglected as a first approximation. To be more precise, we do include the main effect of this correction by taking into account secondary nucleons that have an energy of at least 30% of the primary one. Nucleons with a lower energy give a negligible contribution compared to the primary flux due to its steep energy spectrum Eq. (1). These leading nucleons emerging in the interactions are therefore allowed to generate a

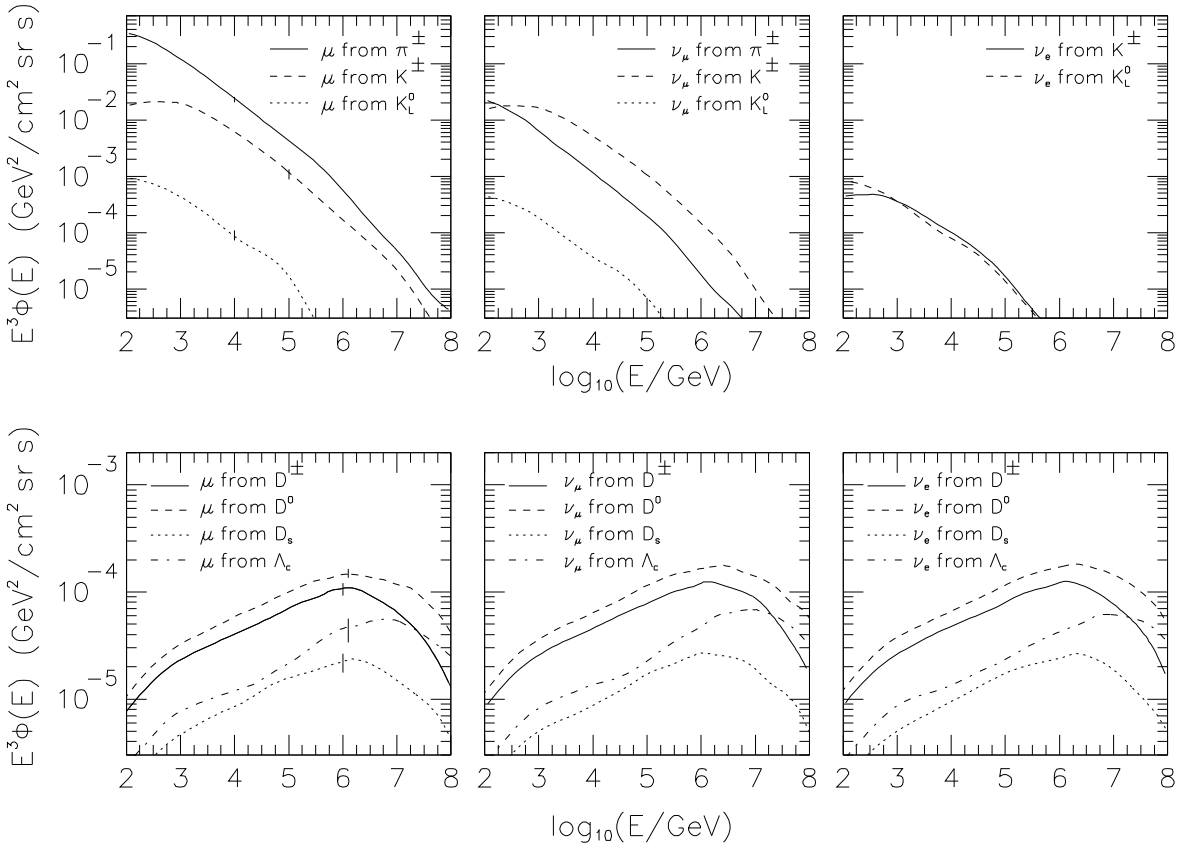

Figure 2: *The E^3-weighted flux of muons ($\mu^+ + \mu^-$), muon-neutrinos ($\nu_\mu + \bar{\nu}_\mu$) and electron-neutrinos ($\nu_e + \bar{\nu}_e$) from decays of the specified particles. The error bars indicate the statistical precision of the Monte Carlo simulation.*

secondary interaction at a height

$$h = -h_0 \ln\left(e^{-H/h_0} - \frac{\lambda_N \ln R'}{X_0}\right), \tag{16}$$

obtained analogously to Eq. (15) but taking into account the finite height H of the primary interaction. The procedure is iterated until the energy of the leading nucleon from an interaction falls below 30% of the primary cosmic ray proton energy.

Secondary mesons and unstable baryons are traced through the atmosphere until they either decay or interact. Which of these occurs is decided by comparing simulated decay and interaction lengths

$$L_{dec} = -d_M(E) \ln R_1 \tag{17}$$

and

$$L_{int} = H + h_0 \ln\left(e^{-H/h_0} - \frac{\lambda_M \ln R_2}{X_0}\right), \tag{18}$$

where R_1 and R_2 denote uniform random numbers $\in]0,1[$ and H is the height at which the traced particle has been produced. The decay length $d_M(E)$ and the interaction thickness λ_M are given in Eqs. (11) and (8) respectively, the atmospheric scale height h_0 and depth X_0 are defined in sect. 2.2. Eq. (18) is obtained in a way analogous to Eq. (16).

Particle decays are fully simulated with daughter particle momenta. In case of interactions, the interacting particle is regenerated in the same direction but with degraded energy, chosen according to the appropriate leading particle spectrum. Considering only the most energetic 'leading' particles in secondary interactions is justified because they give the dominant contribution to the lepton fluxes. Moreover, other particles with lower energy are much fewer than the particles of the same type and energy produced in primary interactions.

The particle decay–interaction chain is then repeated until all particles have decayed, have hit the ground or their energy has fallen below the minimum energy of interest, 100 GeV. Energy

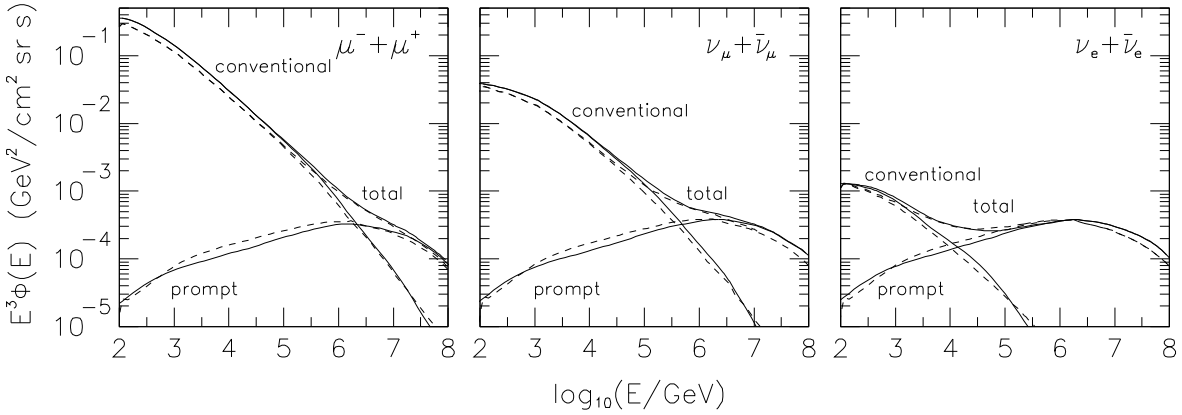

Figure 3: *The E^3-weighted vertical flux of muons, muon-neutrinos and electron-neutrinos from conventional (π, K decays) and prompt (charm decays) sources and their sum ('total'). The solid lines are from the cascade simulation (section 3) and the dashed lines are from the analytic Z-moment method (section 4).*

		N_0	γ	A	E_0	γ'	N_0'
Conventional	$\mu^- + \mu^+$	$2.0 \cdot 10^{-1}$	1.74	$7.0 \cdot 10^{-3}$	$5.3 \cdot 10^5$	2.10	$2.2 \cdot 10^1$
Prompt	$\mu^- + \mu^+$	$1.4 \cdot 10^{-5}$	1.77	$2.8 \cdot 10^{-8}$	$9.2 \cdot 10^5$	2.01	$4.3 \cdot 10^{-4}$
Conventional	$\nu_\mu + \bar{\nu}_\mu$	$1.2 \cdot 10^{-2}$	1.74	$2.0 \cdot 10^{-3}$	$6.3 \cdot 10^5$	2.17	$3.8 \cdot 10^0$
Prompt	$\nu_\mu + \bar{\nu}_\mu$	$1.5 \cdot 10^{-5}$	1.77	$3.1 \cdot 10^{-8}$	$1.2 \cdot 10^6$	1.99	$3.1 \cdot 10^{-4}$
Conventional	$\nu_e + \bar{\nu}_e$	$4.2 \cdot 10^{-4}$	1.63	$7.0 \cdot 10^{-3}$	$5.0 \cdot 10^4$	2.12	$8.4 \cdot 10^{-2}$
Prompt	$\nu_e + \bar{\nu}_e$	$1.5 \cdot 10^{-5}$	1.77	$3.0 \cdot 10^{-8}$	$1.2 \cdot 10^6$	2.02	$4.9 \cdot 10^{-4}$

Table 1: *Values of parameters in Eq. (19) obtained from fits to the Monte Carlo results of the cascade simulations in Fig. 3.*

spectra for muons and neutrinos are finally obtained by counting muons and neutrinos with the initially-assigned primary proton weight.

The resulting fluxes of muons and neutrinos from different parent particles are shown in Fig. 2. For charmed particles the figure clearly demonstrates the dominance of the $D^{\pm,0}$ mesons, while for conventional fluxes the dominant source varies with the type of lepton considered. Summing the various contributions gives the inclusive fluxes in Fig. 3. As can be seen, the prompt contribution from charmed particles dominates at high energies.

The results for the inclusive prompt and conventional fluxes can be parametrised as (similarly to [7], cf. with the primary flux and Eq. (38) below)

$$\phi(E) = \begin{cases} N_0\, E^{-\gamma-1}/(1 + A\, E)\,, & E < E_0, \\ \\ N_0'\, E^{-\gamma'-1}/(1 + A\, E)\,, & E > E_0, \end{cases} \tag{19}$$

with an accuracy of typically better than 10% using the fitted parameter values in Table 1.

4 Approximate analytic solutions

Approximate analytic expressions for the muon and neutrino fluxes can be found from the cascade equations in sect. 2.4 by interpolation of high-energy and low-energy asymptotic solutions. This is done in the standard treatment for power law primary spectra and scale-invariant interaction cross sections [1, 7, 9]. We wish to generalize the standard treatment to include non-scaling effects.

The cascade equations for nucleons and mesons (and unstable baryons) can, using Eqs. (9,10, 12), be written

$$\frac{\mathrm{d}\phi_N}{\mathrm{d}X} = -\frac{\phi_N}{\lambda_N} + Z_{NN}\frac{\phi_N}{\lambda_N}, \tag{20}$$

$$\frac{\mathrm{d}\phi_M}{\mathrm{d}X} = -\frac{\phi_M}{\rho d_M} - \frac{\phi_M}{\lambda_M} + Z_{MM}\frac{\phi_M}{\lambda_M} + Z_{NM}\frac{\phi_N}{\lambda_N}, \tag{21}$$

where the spectrum-weighted moments for generation Z_{NM} and regeneration Z_{NN}, Z_{MM} in hadronic collisions are generally defined as

$$Z_{kh} = \int_E^\infty \mathrm{d}E'\, \frac{\phi_k(E', X, \theta)}{\phi_k(E, X, \theta)}\, \frac{\lambda_k(E)}{\lambda_k(E')}\, \frac{\mathrm{d}n(kA \to hY; E', E)}{\mathrm{d}E}. \tag{22}$$

It is assumed that the fluxes of nucleons, mesons, unstable baryons, muons and neutrinos can be approximated in the factorized form $\phi_i(E, X, \theta) = E^{-\beta_i}\, \phi_i(X, \theta)$, with appropriate values of

the exponents β_i in the low- and high-energy asymptotic regimes. We consider both a primary spectrum $\phi_N(E) \propto E^{-\gamma-1}$ with a constant spectral index γ, and the primary spectrum with a knee as given in Eq. (1). Since nucleon and meson fluxes develop rapidly in the atmosphere, their ratios are essentially independent on the depth X. To a good approximation one therefore obtains the *energy-dependent* spectrum-weighted moments

$$Z_{kh}(E) = \int_E^\infty \mathrm{d}E' \left(\frac{E'}{E}\right)^{-\gamma-1} \frac{\lambda_k(E)}{\lambda_k(E')} \frac{\mathrm{d}n(kA \to hY; E', E)}{\mathrm{d}E}, \tag{23}$$

which we will estimate numerically. In previous studies it has been assumed that Feynman scaling holds, such that the distributions in $x_F = E_h/E_k$ of produced particles are energy independent (cf. Eq. (7)). With this additional assumption the Z-moments become simply

$$Z_{kh}^{scaling} = \int_0^1 x_F^\gamma \frac{\mathrm{d}n_{kh}}{\mathrm{d}x_F} \mathrm{d}x_F. \tag{24}$$

We will not make this scaling assumption, but investigate its validity by our calculation of the energy-dependent Z-moments.

An approximate solution for the nucleon fluxes is then

$$\phi_N = e^{-X/\Lambda_N}\, \phi_N(E), \tag{25}$$

where the nucleon attenuation length Λ_N is defined as

$$\Lambda_N(E) = \frac{\lambda_N(E)}{1 - Z_{NN}(E)}, \tag{26}$$

and $\phi_N(E)$ is the primary nucleon spectrum.

Concerning mesons and unstable baryons, at sufficiently low energies the interaction term can be neglected and so also the regeneration term. One then finds

$$\phi_M^{low} = \frac{Z_{NM}}{1 - Z_{NN}} \frac{\rho d_M}{\Lambda_N} e^{-X/\Lambda_N}\, \phi_N(E). \tag{27}$$

In the high energy regime it is the decay term that can be neglected, and one finds in a similar way

$$\phi_M^{high} = \frac{Z_{NM}}{1 - Z_{NN}} \frac{e^{-X/\Lambda_M} - e^{-X/\Lambda_N}}{1 - \Lambda_N/\Lambda_M}\, \phi_N(E), \tag{28}$$

with the meson attenuation length Λ_M defined analogously to Eq. (26). Notice that at high energies the spectral index of the meson flux is the same as that of the primary flux, $\phi_M^{high} \propto E^{-\gamma-1}$, while at low energies the meson spectrum is flatter by one power of energy, $\phi_M^{low} \propto E^{-\gamma}$, because of the implicit proportionality of the decay length d_M to the energy E.

The spectrum-weighted moments for hadron generation in hadron–air collisions can be rewritten as

$$Z_{kh}(E_h) = \int_{E_h}^\infty \mathrm{d}E_k \frac{\sigma_{kA}(E_k)}{\sigma_{kA}(E_h)} \left(\frac{E_k}{E_h}\right)^{-\gamma-1} \frac{\mathrm{d}n(kA \to hY; E_k, E_h)}{\mathrm{d}E_h}. \tag{29}$$

The numerical evaluation of these Z-moments was made by applying the prefactor in the integrand to the hadron spectra $\mathrm{d}n_{kh}/\mathrm{d}E_h$ generated at different incoming energies E_k between 10^2 and 10^9 GeV with the Pythia Monte Carlo (see section 5 for details on the generation mechanism). Total inelastic cross sections $\sigma_{kA}(E)$ in Eq. (29) were taken from ref. [33] when available. The spectra of regenerated kaons and D mesons, which cannot be used as beam particles in

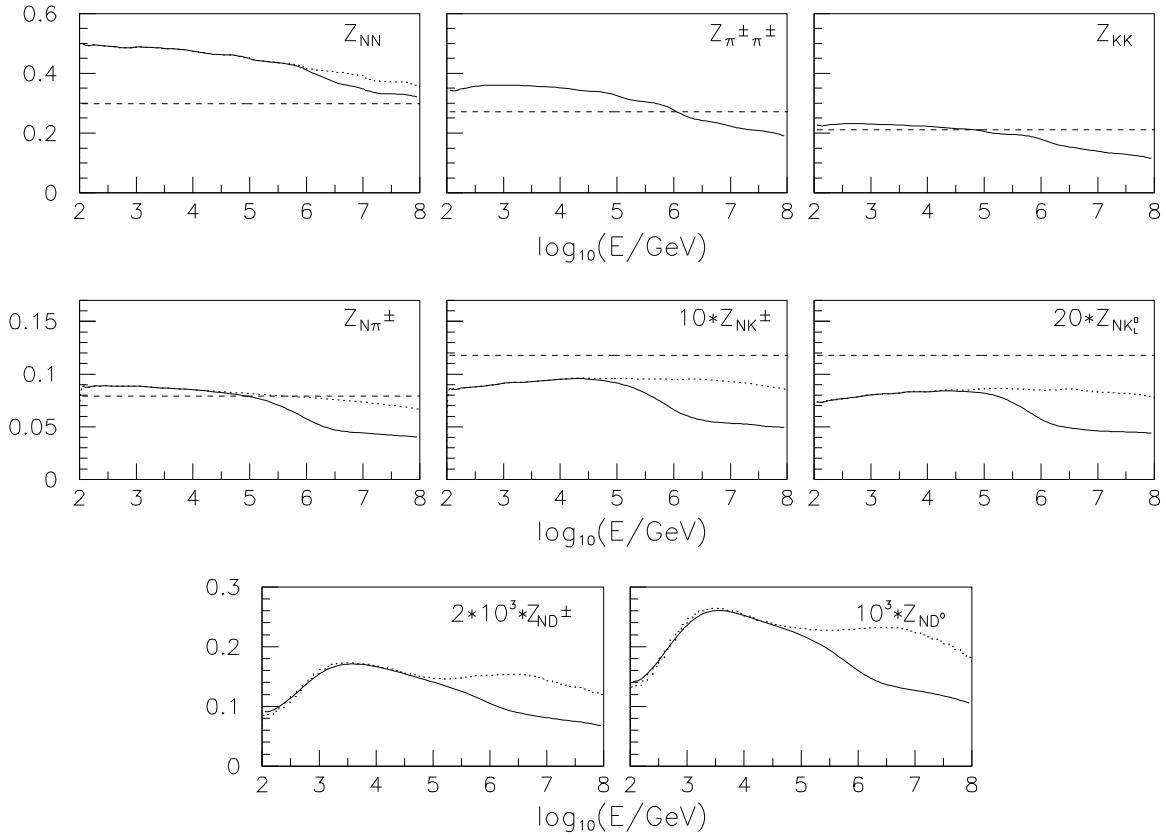

Figure 4: *Energy-dependence of production Z_{kh}-moments, Eq. (29), for incoming particle k producing hadron h. Solid lines are the results of our model using the initial spectrum with a 'knee', Eq. (1), whereas the dotted lines are obtained with a constant spectral index $\gamma = 1.7$. Dashed lines show the values of [9] based on Feynman scaling.*

Pythia simulations, were approximated by the leading pion spectrum obtained in pion-proton collisions. Regeneration of Λ_c-baryons was mimicked using an ordinary Λ as a beam particle in Pythia and extracting the spectrum of leading Λ's. The resulting muon and neutrino spectra are rather insensitive to these approximations, since they are slowly varying functions of kaon and heavier hadron regeneration Z-moments (they enter only through the combination A_M in Eq. (39) below).

For the charm Z-moments one has to consider that the charm cross section need not scale with the target atomic number A in the same way as the total inelastic cross section. The ratio of the A^1-dependence in our charm cross section (see section 5.2) and the inclusive $A^{2/3}$-dependence (see section 2.3) gives a $A^{1/3}$-dependence in the Z-moments for charm, which are included in our results (*e.g.* Fig. 4).

The energy dependence of the hadron generation and regeneration Z-moments is shown in Fig. 4 for a constant spectral index $\gamma = 1.7$ (dotted lines) and for a primary spectrum with a knee as in Eq. (1) (solid lines). For comparison, we also show the constant values given by Lipari [9] under the assumptions of energy-independent inelastic cross sections and Feynman scaling of the meson spectra [34, 35], i.e. with a Z-moment defined by Eq. (24). It is clear

Particle	$\pi^{\pm}$	$K^{\pm}$	K_L	$D^{\pm}$	D^0	Λ_c	D_s	J/ψ
ε [GeV]	115	850	205	$3.74 \cdot 10^7$	$9.47 \cdot 10^7$	$2.57 \cdot 10^8$	$9.33 \cdot 10^7$	$8.8 \cdot 10^{15}$

Table 2: *Critical energies for hadrons traversing the atmosphere in the vertical direction.*

from the figures that variations of the Z-moments with energy are non-negligible, in particular when the changing slope (γ) of the primary spectrum is included. On the other hand, this energy dependence of the Z-moments, and of the interaction lengths λ, is mild with respect to the rapid decrease of the primary flux with increasing energy. For example, differentiation of Eq. (25) gives

$$\frac{E}{\phi_N}\frac{\mathrm{d}\phi_N}{\mathrm{d}E} = \frac{X}{\Lambda_N}\frac{E}{\Lambda_N}\frac{\mathrm{d}\Lambda_N}{\mathrm{d}E} - (\gamma+1), \tag{30}$$

where the first term comes from the energy dependence of Z and λ and the second term from the primary spectrum. Numerically, the former is only 0.1, much smaller than the latter which is 2.7 or 3.0. This demonstrates that the treatment of non-scaling effects as corrections embodied through energy-dependent Z-moments is justified irrespectively of the derivation leading to Eq. (23).

We can now find approximate asymptotic solutions for the muon and neutrino fluxes. In the asymptotic regimes meson fluxes are well approximated by power laws, $\phi_M(E) \propto E^{-\beta}$, with $\beta = \gamma$ in the low energy case and $\beta = \gamma + 1$ in the high energy case. Hence the source terms in the lepton cascade equation (Eq. 13)) can be rewritten as

$$S(M \to \ell Y) = Z_{M\to\ell,\beta+1}\frac{\phi_M}{\rho d_M}, \tag{31}$$

with decay spectrum-weighted moments defined by[4]

$$Z_{M\to\ell,\beta+1} = \int_E^\infty \mathrm{d}E_M \left(\frac{E_M}{E}\right)^{-\beta} \frac{d_M(E)}{d_M(E_M)}\frac{\mathrm{d}n(M\to\ell Y; E_M, E)}{\mathrm{d}E}. \tag{32}$$

Integrating the lepton cascade equations over the line of sight, one then obtains the following expressions for the lepton fluxes deep in the atmosphere ($X \to \infty$):

$$\phi_\ell^{low} = Z_{M\to\ell,\gamma+1}\frac{Z_{NM}}{1-Z_{NN}}\phi_N(E) \tag{33}$$

for leptons coming from low energy mesons and

$$\phi_\ell^{high} = Z_{M\to\ell,\gamma+2}\frac{Z_{NM}}{1-Z_{NN}}\frac{\ln(\Lambda_M/\Lambda_N)}{1-\Lambda_N/\Lambda_M}\frac{\varepsilon_M}{E}\phi_N(E) \tag{34}$$

for leptons coming from high energy mesons (with $E_M \gg m_M$). In Eq. (34), ε_M is a critical meson energy separating the low energy and the high energy regimes, *i.e.* where the meson dominantly decays or interacts, respectively. It depends on the atmospheric profile and in general on zenith angle. For the exponential atmospheric profile in sect. 2.2 and in the vertical direction, one has [1]

$$\varepsilon_M = \frac{m_M c^2 h_0}{c\tau_M}. \tag{35}$$

[4]To keep the analogy with the (re)generation Z-moments, which include the multiplicity of the final state, we include the branching ratio $\mathrm{Br}(M \to \ell X)$ into the definition of the decay Z-moments. This differs from [9].

	$\beta = 1.7$	$\beta = 2$	$\beta = 2.7$	$\beta = 3$
$\pi^\pm \to \mu^-/\mu^+$	0.675	0.634	0.553	0.523
$K^\pm \to \mu^-/\mu^+$	0.253	0.227	0.183	0.169
$K^0_L \to \mu^-/\mu^+$	0.0543	0.0435	0.0273	0.0227
$D^\pm \to \mu^-/\mu^+$	0.0171	0.0124	0.00636	0.00490
$D^0 \to \mu^-/\mu^+$	0.00880	0.00651	0.00346	0.00270
$D_s \to \mu^-/\mu^+$	0.00708	0.00516	0.00266	0.00205
$\Lambda_c \to \mu^-/\mu^+$	0.00377	0.00269	0.00130	0.000976
$J/\psi \to \mu^- + \mu^+$	0.045	0.040	0.033	0.030
$\pi^\pm \to \nu_\mu/\bar{\nu_\mu}$	0.0870	0.0607	0.0271	0.0194
$K^\pm \to \nu_\mu/\bar{\nu_\mu}$	0.221	0.196	0.153	0.139
$K^0_L \to \nu_\mu/\bar{\nu_\mu}$	0.0292	0.0216	0.0115	0.00894
$D^\pm \to \nu_\mu/\bar{\nu_\mu}$	0.0181	0.0134	0.00720	0.00566
$D^0 \to \nu_\mu/\bar{\nu_\mu}$	0.00839	0.00636	0.00354	0.00283
$D_s \to \nu_\mu/\bar{\nu_\mu}$	0.00744	0.00550	0.00292	0.00228
$\Lambda_c \to \nu_\mu/\bar{\nu_\mu}$	0.00395	0.00284	0.00141	0.00107
$K^\pm \to \nu_e/\bar{\nu_e}$	0.00653	0.00509	0.00298	0.00242
$K^0_L \to \nu_e/\bar{\nu_e}$	0.0517	0.0401	0.0235	0.0191
$D^\pm \to \nu_e/\bar{\nu_e}$	0.0187	0.0139	0.00756	0.00597
$D^0 \to \nu_e/\bar{\nu_e}$	0.00870	0.00660	0.00372	0.00298
$D_s \to \nu_e/\bar{\nu_e}$	0.00767	0.00571	0.00306	0.00240
$\Lambda_c \to \nu_e/\bar{\nu_e}$	0.00404	0.00293	0.00148	0.00101

Table 3: *Decay Z-moments $Z_{M\to\ell,\beta+1}$ for various decay channels. (For the decay $J/\psi \to \mu^- + \mu^+$ a factor 2 is included to account for both μ^- and μ^+.)*

In Table 2 we have collected the critical energies ε_M used in this study. For not too large zenith angles $\theta \lesssim 60°$, Eq. (3) leads to $\varepsilon_M \propto 1/\cos\theta$ and ϕ_ℓ^{high} depends on the zenith angle.

To resume, the lepton fluxes from meson M have the same spectral index of the primary flux, $\phi_\ell^{low} \propto E^{-\gamma-1}$, and are independent of zenith angle at energies smaller than the meson critical energy ε_M, while they are steeper by one power of energy and depend on zenith angle at energies above ε_M, $\phi_\ell^{high} \propto E^{-\gamma-2}/\cos\theta$. We see that at the energies of interest to us, pions and kaons are above their critical energy and so generate 'conventional' muons and neutrinos, while charmed mesons are below their critical energy ($\sim 10^7$ GeV) and give 'prompt' muons and neutrinos.

The energy spectra of muons and neutrinos from decays of ultra-relativistic mesons take a simple scaling form [9]

$$\mathrm{d}n(M \to \ell Y; E_M, E) = F_{M\to\ell}\left(\frac{E}{E_M}\right)\frac{\mathrm{d}E}{E_M}, \tag{36}$$

and the decay Z-moments are independent of energy

$$Z_{M\to\ell,\beta+1} = \int_0^1 \mathrm{d}x\, x^\beta\, F_{M\to\ell}(x)\,, \tag{37}$$

with $x = E/E_M$. Approximate expressions for the functions $F_{M\to\ell}$ have been obtained for two and three body decay channels in ref. [9].[5] Since there are many semi-leptonic decay channels

[5]Because of our convention, the functions $F_{M\to\ell}$ in ref. [9] should be multiplied by the branching ratio Br $(M \to \ell\, X)$.

for charmed mesons and most of them have more than three particles in the final state, we prefer to generate all decay spectra within the Lund Monte Carlo. In Table 3 we list the values of the decay Z-moments for the spectral indices of interest in this study.

Finally we join the low and high energy solutions with the interpolation

$$\phi_\ell = \sum_M \frac{\phi_\ell^{low}\phi_\ell^{high}}{\phi_\ell^{low}+\phi_\ell^{high}} = \frac{\phi_N(E)}{1-Z_{NN}} \sum_M \frac{Z_{NM}Z_{M\to\ell,\gamma+1}}{1+A_M E/\varepsilon_M}, \tag{38}$$

with

$$A_M = \frac{Z_{M\to\ell,\gamma+1}}{Z_{M\to\ell,\gamma+2}} \frac{1-\Lambda_N/\Lambda_M}{\ln(\Lambda_M/\Lambda_N)}. \tag{39}$$

The fluxes of muons and neutrinos calculated according to Eq. (38) using the previously-obtained energy-dependent Z-moments are plotted in Fig. 3 as dashed lines. It is satisfying to see that the cascade simulations and the approximate analytic solutions, which are conceptually rather different, give results that are quite close. Detailed comparison of corresponding fluxes shows good agreement both for conventional and prompt muons and neutrinos. The differences are typically less than 20% which is quite sufficient in this context. For the prompt leptons, this is below the uncertainty in our charm calculation (see section 5) and far smaller than the differences between the different models discussed in section 7.

5 The model for particle production

A model for particle production is needed to specify the energy spectra of secondaries in cosmic ray collisions with atmospheric nuclei. As discussed in section 2.3, collisions involving nuclei can be reduced to the simpler proton-nucleon collision. This applies in particular when only energetic particles are of interest, as in our case.

The flux of conventional muons and neutrinos results from the decay of relatively long-lived particles, such as π and K mesons. The production of such hadrons, containing only light quarks (u, d, s), is dominated by minimum bias proton-nucleon interactions (without large momentum transfers) and receives a small contribution from diffractive interactions. On the other hand, the prompt muons and neutrinos arise through decays of short-lived particles, *i.e.* dominantly charmed particles. Charm quarks are, due to their relatively large mass, usually considered to be produced in hard processes which can be described by perturbative QCD (pQCD). In the following, some relevant details of the models implemented in the Pythia and Jetset Monte Carlo programs [31] will be discussed. The hypothetical non-perturbative intrinsic charm mechanism is discussed separately in section 6.

5.1 Light particle production

The production of light hadrons is dominantly through minimum bias hadron-hadron collisions. The strong interaction mechanism is here of a soft non-perturbative nature that cannot be calculated based on proper theory, but must be modelled. In the successful Lund model [32] hadron production arise through the fragmentation of colour string fields between partons scattered in semi-soft QCD interactions [31]. The essentially one-dimensional colour field arising between separated colour charges is described by a one-dimensional flux tube whose dynamics is taken as that of a massless relativistic string. Quark-antiquark pairs are produced from the energy in the field through a quantum mechanical tunneling process. The string is thereby broken into smaller pieces with these new colour charges as endpoints and, as the process is iterated,

primary hadrons are formed. These obtain limited momenta transverse to the string (given by a Gaussian of a few hundred MeV width) but their longitudinal momentum may be large as it is given by a probability function in the fraction of the available energy-momentum in the string system taken by the hadron. The iterative and stochastic nature of the process is the basis for the implementation of the model in the JETSET program [31].

A non-negligible contribution to the inclusive cross section is given by diffractive interactions. These are also modeled in PYTHIA [31] using cross sections from a well functioning Regge-based approach and simulating the diffractively produced final state using an adaptation of the Lund string model. These diffractive events are included in our simulations and contribute rather less than 10% to the final results.

5.2 Perturbative production of charm

Charm production is strongly suppressed in hadronisation models that are commonly used in detailed comparisons with experimental data on multihadron production in various high energy collisions. The tunneling mechanism in the Lund model [32] gives a production probability of different quark flavours as $u\bar{u} : d\bar{d} : s\bar{s} : c\bar{c} \simeq 1 : 1 : 0.3 : 10^{-11}$, *i.e.* charm production in the hadronization phase can here be safely neglected.

Charm quarks are instead considered to be produced in perturbative QCD processes in accordance with the relatively large charm quark mass. To leading order (LO) in the coupling constant, *i.e.* $\mathcal{O}(\alpha_s^2)$, these are the gluon-gluon fusion process $gg \to c\bar{c}$ and the quark-antiquark annihilation process $q\bar{q} \to c\bar{c}$ as shown in Fig. 5abc. The charm production cross section is calculated using the usual convolution of parton densities f_i in the colliding hadrons and the hard parton level cross section $\hat{\sigma}$ from pQCD, *i.e.*

$$\sigma = \int\int\int dx_1 dx_2 d\hat{t} \;\; f_1(x_1, Q^2)\; f_2(x_2, Q^2)\; \frac{d\hat{\sigma}}{d\hat{t}} \tag{40}$$

Here, x_i are the parton longitudinal momentum fractions in the hadrons and $\hat{t}$ is the Mandelstam momentum transfer at the parton level. Q^2 is the factorization scale defining at what momentum transfer the parton densities are probed and also regulating the amount of pQCD scaling violations; we have used $Q^2 = (m^2_{\perp c} + m^2_{\perp \bar{c}})/2$, where $m^2_\perp = m^2 + p^2_\perp$. The charm quark mass introduces a threshold in the invariant mass of the parton level subsystem, *i.e.* $\hat{s} = x_1 x_2 s > 4m_c^2 c^4$. The dominating contribution to the cross section comes from the region close to this threshold, since $d\sigma/d\hat{s}$ is a steeply falling distribution. It is therefore important to use QCD matrix elements with the charm quark mass explicitly included. The numerical value used is $m_c = 1.35\, GeV/c^2$ together with $\Lambda_{QCD} = 0.25\, GeV$ (in accordance with using the $MRSG$ parton density parametrisation [36]).

Next-to-leading order (NLO), *i.e.* $\mathcal{O}(\alpha_s^3)$, cross sections for heavy flavour production in hadron collisions have been calculated in pQCD [37, 38]. Compared to the leading order results there is an overall increase of the cross section of about a factor of two. This does not demonstrate a bad convergence of the perturbative series, since the main NLO contribution is associated with a process that does not appear in leading order charm production. This is the gluon scattering process $gg \to gg$, which has a much larger cross section than the leading order charm processes and is of a comparable magnitude when including the NLO correction $g \to c\bar{c}$ shown in Fig. 5d. Since the NLO distributions of the charm quark transverse momentum and rapidity to a reasonable approximation have the same shape as the LO ones, we take the NLO results into account by rescaling the cross section with an overall factor $K = 2$. Still higher order corrections have not been calculated, but their effect should be significantly smaller since

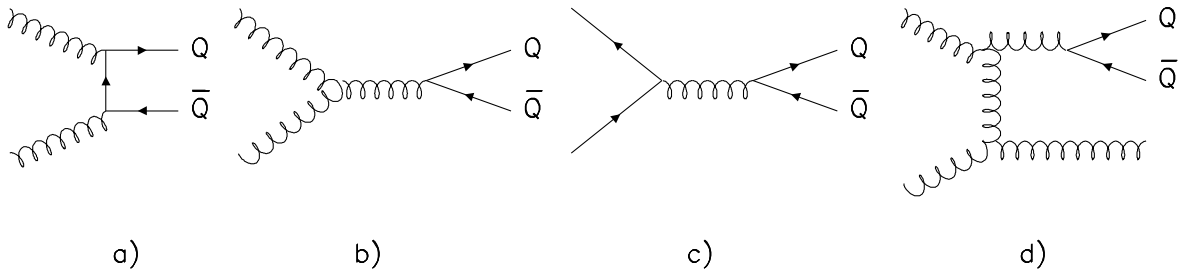

Figure 5: *Illustration of charm production in pQCD. The leading order processes (a,b,c) and an important next-to-leading order process (d).*

there should be no such additional process entering like for NLO. The factor $K = 2$ is indeed consistent when comparing the leading order cross sections with experimental results [39].

Another estimate of higher order corrections can be obtained from charm production in the simulated parton cascades implemented in PYTHIA. These represent a leading logarithm approximation of multiple parton emission from the incoming and scattered partons in basic QCD $2 \to 2$ processes. Charm quark production arises here through the perturbative QCD gluon splitting process $g \to c\bar{c}$, *i.e.* basically the same as in the NLO matrix element calculation. This approximate charm production to arbitrary order in pQCD gives a contribution of the same magnitude as the LO matrix elements, thus confirming the use of a renormalisation factor of $K = 2$. Furthermore, the energy spectra of the charm quarks from this higher order treatment are very similar to those from the LO calculation. If anything, they rather tend to be slightly softer than the LO distribution [6]. Since it is the hardest part of the spectrum that gives the largest contribution to the high energy neutrino and muon spectra, one may conclude that taking the higher order corrections into account through a global K-factor renormalisation and keeping the leading-order shape of the charm quark energy spectra, as we have done, is sufficient for the precision needed in this study.

The charm production cross section depends on the input for the parton density functions $f_i(x_i, Q^2)$ in Eq. (40). With charm production being dominantly close to threshold $\hat{s} = x_1 x_2 s > 4m_c^2 c^4$, the typical initial momentum fractions x_i will decrease with increasing collision energy s. This is demonstrated in Fig. 6, which shows the distribution of initial parton momentum fractions in charm production at different energies. At the highest energies, the parton densities are probed down to $x \sim 10^{-5}$ or even below. The recent data from the *ep* collider HERA [40, 41] show a significant increase at small x, $xf(x) \sim x^{-a}$ and constrain the parton densities down to $x \sim 10^{-4}$. These data, together with other data from previous deep inelastic scattering experiment as well as other processes, have been used in the parametrization $MRSG$ [36] of parton densities. The resulting small-x behaviour is given by the power $a = 0.07$ for sea quarks and $a = 0.30$ for gluons. Since $MRSG$ is the most recent parametrisation, using essentially all relevant experimental data, we use this as our standard choice. To investigate [6] the dependence on the choice of parton density parametrisations, we also applied the $MRSD_0$ [42] with the small-x behavior $x\,f(x) \sim const$, which before the HERA data was an acceptable parametrisation. The effect on the total charm production cross section from the choice of parton density parametrisation is illustrated in Fig. 7 with curves resulting from these parametrisations. At high energy there

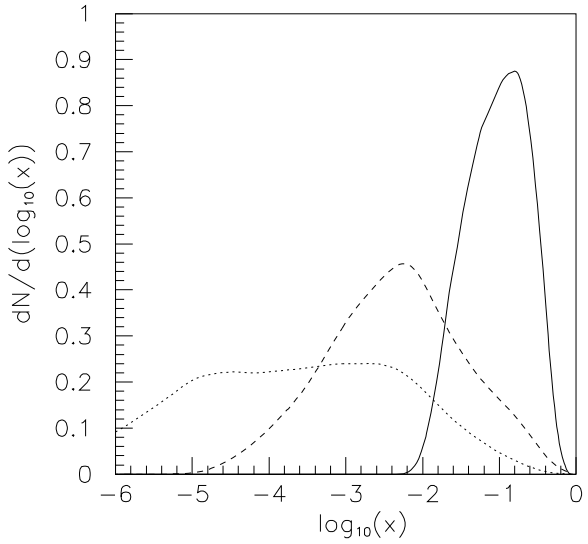

Figure 6: *Distribution of momentum fraction x for the initial partons entering the QCD charm production subprocesses. The curves represent three different beam particle energies:* 10^3 *GeV (solid),* 10^6 *GeV (dashed) and* 10^9 *GeV (dotted).*

is a large dependence on the choice of parton density functions. The difference between the G and the D_0 parametrisations should however not be taken as a theoretical uncertainty. First of all the D_0 parametrisation is known to be significantly below the small-x HERA data and gives therefore a significant underestimate at large energies. Secondly, the naive extrapolation of the G parametrisation below the measured region $x \gtrsim 10^{-4}$ at rather small Q^2 ($\sim m_c^2$) leads to an overestimate. A flatter dependence like $x^{-\epsilon}$ with $\epsilon \simeq 0.08$ as $x \to 0$ can be motivated ([43] and references therein) based on a connection to the high energy behaviour of cross sections in the Regge framework. The implementation of this approach in PYTHIA makes a smooth transition to this dependence such that the parton densities are substantially lowered for $x \lesssim 10^{-4}$ leading to a substantial reduction of the charm cross section at large energies, as given by the solid curve in Fig. 7.

Using this procedure we get a quite decent agreement between experimental charm production data and the PYTHIA simulation results over a wide range of energies (Fig. 7). A few comments on the data in Fig. 7 are here in order. A given experiment is only sensitive to some channels and a limited kinematical region. The total charm cross section is therefore obtained by a rescaling with charm decay branching ratios and by using assumed shapes of the x_F distributions to extrapolate to unmeasured regions. In particular, corrections to points 1,2,6 and 7 are small while they are large for point 9 and 13. The bands 8,10,11 and 12 illustrates the uncertainty in these experiments due to this extrapolation. In band 8 the uncertainty includes a scaling for including $D^{\pm}$-mesons (taken from [49, 51]). Data-band 11 is based on $D^+\bar{D}$ identification, 12 on $\Lambda_c^+\bar{D}$ and 10 on Λ_c^+ identification. Furthermore, points 3, 4 and 5 are from beam dump experiments on heavy nuclear targets without direct charm identification and have an additional uncertainty from the scaling with nuclear number. In point 4 the scaling $A^{0.75}$ has been assumed, which we have rescaled in 4' to a A^1-dependence in order to be consistent with the other beam dump experiments and with our model. Data points 2 and 6 come from

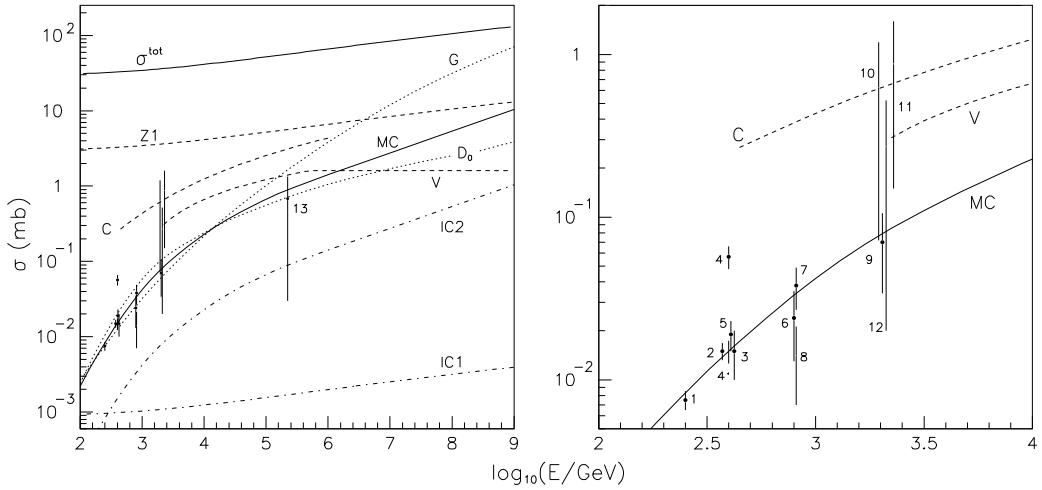

Figure 7: *Energy dependence of charm production cross section in $pp(p\bar{p})$. The experimental data points are 1:[44] 2:[45], 3:[46], 4,4':[47], 5:[48], 6:[49], 7:[50], 8:[51] 9:[52], 10:[53], 11:[54, 55], 12:[56, 55] and 13:[57]. The solid line is the result of our model. The dotted lines result from a naive application of the MRS parametrisations G and D_0 of parton densities. The dashed lines represent earlier models, C from [15], V from [17] and Z1 from [20] which is 10% of the total pp cross section σ^{tot}. The curves IC1 and IC2 are based on the intrinsic charm hypothesis (section 6). Detailed discussions are in sections 5.2 and 7.*

pp interactions with explicit charm particle identification. Although these issues leave some uncertainty for each individual result, the combination of all data should give a trustworthy knowledge on the charm cross section and its energy dependence.

As indicated, there is an uncertainty related to the dependence of the charm production cross section on the nuclear mass A. Since the discussed pQCD charm production involves hard scattering processes with a small cross section, one may argue that it does not only take place with nucleons at the nuclear surface but also with nucleons in the interior. Consequently, the power α_c in $\sigma(pA \to c\bar{c}) = A^{\alpha_c}\sigma(pN \to c\bar{c})$ may be larger than 2/3 and rather be 1, corresponding to interactions in the whole nucleus. In fact, experiments give values of α_c that are mainly close to 1 (see *e.g.* [63] and references therein), which is the value we have adopted in our calculations. This is also in agreement with a number of recent experiments with both pion and proton beams [51, 58, 59]. Using $\alpha_c = 2/3$ instead would lead to a reduction of the normalisation for the prompt muon and neutrino fluxes by the factor $A^{2/3}/A = 14.5^{-1/3} \approx 0.4$. This is at most an upper bound for the uncertainty of the A-dependence.

5.3 Semileptonic decays of charmed hadrons

The branching ratios for semileptonic charm decays used are $BR(D^{\pm} \to e/\mu) = 17\%$, $BR(D^0 \to e/\mu) = 8\%$, $BR(D_s^{\pm} \to e/\mu) = 8\%$, $BR(\Lambda_c^+ \to e/\mu) = 4.5\%$. These values agree with experimental measurements as compiled by the 'Particle Data Group' [33]. To distribute momenta in the charm hadron decay $H \to \ell\nu_\ell h$, the Monte Carlo [31] uses the weak $V - A$ matrix element

$$|\mathcal{M}|^2 = (p_H p_\ell)(p_\nu p_h) \tag{41}$$

in terms of the involved four-vectors and neglecting decay product masses. H is the charm hadron and h is the final hadron in a three-body decay and generalized to represent the final state hadron system in case of more final hadrons. The multiplicity and momenta within the h-system is phenomenologically modelled [31] and tested against data. These details, however, concern the final hadrons and are not important for our purposes, because we only use the final leptons, which should be well accounted for through the weak decay matrix element (41) and the known branching ratios.

6 Possible non-perturbative origin of charm

Although most of the charm production data from accelerator experiments can be reasonably well understood from pQCD calculations, the uncertainty in the data and the calculations cannot exclude some smaller non-perturbative contribution. Charm production in pQCD is theoretically well defined and only has some limited numerical uncertainty due to parameter values and NLO corrections which, however, can be examined and controlled as discussed above. In contrast, non-perturbative charm production is not theoretically well defined due to the general problems of non-perturbative QCD. In particular, the absolute normalisation has to be taken from comparison with data. Models for non-perturbative charm production exist and some have been used in the context of atmospheric muon and neutrino fluxes, as discussed in section 7. Here, we will investigate the consequences of the hypothesis of intrinsic charm quarks in the nucleon wave function [60]. Although being far from established, this idea has theoretical motivation [60, 61] and some experimental data can be interpreted as giving evidence [62–67]. It is therefore a serious model for a possible additional mechanism for charm production with a non-perturbative origin. The results presented in this section are based on a more general study [68] of intrinsic charm in high energy collisions, to which we refer for more details of our implementation in an explicit model.

The hypothesis of intrinsic charm (IC) amounts to assuming the existence of a $c\bar{c}$-pair as a non-perturbative component in the bound state nucleon [60]. This means that the Fock-state decomposition of, *e.g.*, the proton wave function, $|p\rangle = A|uud\rangle + B|uudc\bar{c}\rangle + ...$, contains a small, but finite, probability B^2 for such an intrinsic quark-antiquark pair. This should be viewed as a quantum fluctuation of the proton state. The normalization of the heavy quark Fock component is the key unknown, although it should decrease as $1/m_Q^2$. Originally, a 1% probability for charm was assumed, but later investigations, *e.g.* [64, 65], indicate a smaller but non-vanishing level.

Viewed in an infinite momentum frame, all non-perturbative and thereby long-lived components must move with essentially the same velocity in order that the proton can 'stay together' for an appreciable time. The larger mass of the charmed quarks then implies that they take a larger fraction of the proton momentum. This can be quantified by applying old-fashioned perturbation theory to obtain the momentum distribution [60]

$$P(p \to uudc\bar{c}) \propto \left[m_p^2 - \sum_{i=1}^{5} \frac{m_{\perp i}^2}{x_i} \right]^{-2} \tag{42}$$

in terms of the fractional momenta x_i of the five partons i in the $uudc\bar{c}$ state. Neglecting the transverse masses of the light quarks in comparison to the charm quark mass results in the momentum distribution

$$P(x_1, x_2, x_3, x_c, x_{\bar{c}}) \propto \frac{x_c^2 x_{\bar{c}}^2}{(x_c + x_{\bar{c}})^2} \delta(1 - x_1 - x_2 - x_3 - x_c - x_{\bar{c}}) \tag{43}$$

which favour large charm quark momenta as anticipated. In fact, one obtains $\langle x_c \rangle = 2/7$ by integrating out the light quark degrees of freedom x_i.

A proton with such an intrinsic $c\bar{c}$ quantum fluctuation can then interact with another hadron such that charmed particles are realised. A hard interaction with such a charm quark is certainly possible, but the cross section is then suppressed both by the small probability of the fluctuation itself and by the smallness of the perturbative QCD interaction. The charm quarks may, however, also be put on shell through non-perturbative interactions that are not strongly suppressed [61]. This may lead to a rate that is large enough to be of potential interest. To estimate these non-perturbative interactions we have constructed a model [68] based on refs. [60, 62, 63].

The formation of charm hadrons can occur through the following mechanisms. The charm (anti)quark can hadronise into a D-meson as described by a normal hadronisation function, similar to those successfully used in $e^+e^- \to c\bar{c}$. Alternatively, the (anti)charm quark can coalesce with another quark or diquark from the $|uudc\bar{c}\rangle$ state to form a hadron. Following [62, 63] we use the recombination probabilities 50% to form a $\overline{D}$-meson and 30% for a Λ_c, in which cases the remaining c or $\bar{c}$ quark is assumed to hadronise separately from the proton remnant. The probability to directly form a J/ψ (*i.e.* the $c\bar{c}$ pair is combined) is taken to be 1%. The momentum of the hadron formed through coalescence is taken as the sum of the corresponding x_i's, *e.g.* $x_{\Lambda_c} = x_c + x_u + x_d$. The momentum distribution is then obtained by folding Eq. (43) with the proper δ function, *e.g.* $\delta(x_{\Lambda_c} - x_c - x_u - x_d)$, and integrating out all extra degrees of freedom. The c or $\bar{c}$ quarks that does not coalesce with spectator partons are hadronised to D-mesons with a normal hadronisation function. Since such a function is quite hard, we here approximate it with a δ-function to let the charm hadron take the whole charm quark momentum given by Eq. (43), which is consistent with low-p_t charmed hadroproduction data [67].

The shapes of the x_F-distributions for the charmed particles are thereby given (see [68]). They are quite hard, in fact harder than those for charm from pQCD, and therefore have the potential to contribute effectively at high energies. As mentioned, the main uncertainty in the intrinsic charm model is the absolute normalization of the cross section and its energy dependence. The magnitude of the cross section has been estimated [63] from data at relatively low energies ($E_p = 200 - 400\,GeV$). Since the process is basically a soft non-perturbative process it may be reasonable to assume that its energy dependence is the same as that for normal inelastic scattering [61, 68]. We therefore take as our first case

$$\text{IC1}: \quad \sigma_{IC}(s) = 3 \cdot 10^{-5} \sigma_{inel}(s) \tag{44}$$

with normalisation from [63] and shown as curve IC1 in Fig. 7. Alternatively, one might argue that there is a stronger energy dependence related to some threshold behavior for putting the charm quarks on their mass shell. We make a very crude model for this by taking the intrinsic charm cross section to be a constant fraction of the pQCD charm cross section

$$\text{IC2}: \quad \sigma_{IC}(s) = 0.1\, \sigma_{pQCD}(s) \tag{45}$$

as shown by curve IC2 in Fig. 7. This is similar to the low energy ($200 - 800\,GeV$) treatement in [62]. The normalisation is here fixed to be the same as IC1 at the low energy where evidence is claimed for intrinsic charm [63]. There is, however, some indication against such an increased cross section, as in IC2, since no evidence for J/ψ from intrinsic charm was found in an experiment [69] at a somewhat higher energy ($800\,GeV$ proton beam).

The dependence on nuclear mass number should (in both cases) essentially be $A^{2/3}$ reflecting the soft nature of the hadron-hadron interaction. Note, that the intrinsic charm quarks can be

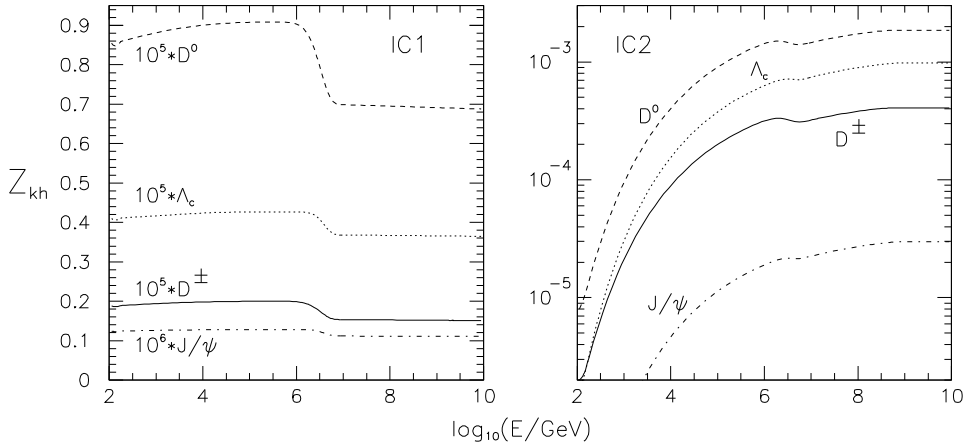

Figure 8: *Energy-dependence of production Z_{kh}-moments, Eq. (29), for incoming particle k = proton producing charmed hadron $h = D^0, D^\pm, \Lambda_c$ and J/ψ through the intrinsic charm mechanism with the two assumed energy dependences IC1 and IC2.*

released through interactions with the other parts of the $|uudc\bar{c}\rangle$ state, as demonstrated clearly in case of J/ψ production after the remaining proton state has been 'stripped off' in the interaction [61].

The intrinsic charm model provides simple and scaling x_F-spectra for the charmed particles which makes the analytic method suitable for calculating the fluxes of muons and neutrinos from their decays. The charm production Z-moments are calculated according to Eq. (29) by numerical integration and shown in Fig. 8. The mild energy dependence of the IC1 case gives essentially constant Z-moments, except for a marked step due to the change of the slope γ in the primary spectrum. The step is more pronounced here compared to charm from pQCD (see Fig. 4) where the x_F-distribution is both energy-dependent and extending to smaller values. The stronger energy dependence in IC2 is reflected in the corresponding Z-moments, where the strong variation at energies below $\sim 10^5\, GeV$ may cast some doubt on the reliability of the analytic method in this region.

The lepton fluxes are then obtained by using Eq. (38) and the regeneration and decay Z-moments calculated in section 4. The results are displayed in Fig. 9 and compared to those from our pQCD calculation. The milder, and more conservative, energy dependence (IC1) of the intrinsic charm cross section gives a result which is only a small ($\sim 10\%$) correction to the pQCD result, except at super-high energies where the rate is extremely small and not measurable in a foreseeable future. Note that the J/ψ contribution is here becoming important, since the J/ψ flux is not attenuated through interactions due to the high critical energy (Table 2). This raises the question of how well the normalisation of the otherwise small J/ψ contribution is known. With the strong energy dependence assumed in IC2, the intrinsic charm result exceeds the pQCD one already at lepton energies around $10^4\, GeV$. Although the energy dependence of this IC2-model is, as mentioned, rather *ad hoc* and may be disfavoured by data, it illustrates the large theoretical uncertainty associated with the intrinsic charm model when extrapolated to the high energies of cosmic ray interactions.

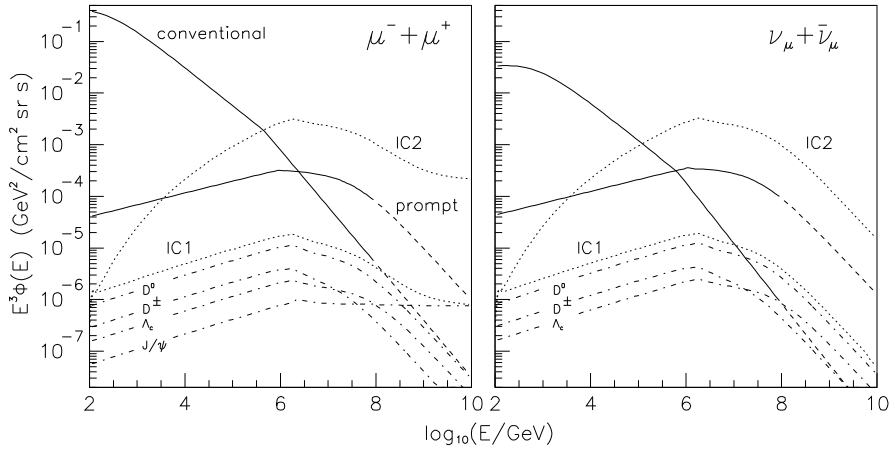

Figure 9: *Fluxes (cf. fig. 3) of muons and neutrinos from the intrinsic charm model with the two assumed energy dependences IC1 and IC2; for IC1 the contributions from different charm particles are given. Shown for comparison are our standard results (full curves) for conventional and prompt fluxes as given by the parametrisation Eq. (19) and extrapolated to higher energies (dashed).*

7 Comparison with previous model calculations

In sections 3 and 4 we have obtained atmospheric muon and neutrino fluxes with two different methods: via a Monte Carlo simulation of the hadronic cascade and via approximate analytical expressions with energy-dependent Z-moments. We were satisfied that the two methods gave consistent results. Here we want to compare our results with those obtained with different models for particle interactions in the atmosphere. In particular, we focus on the prompt muon and neutrino fluxes arising from different charm production mechanisms.

Earlier calculations of the conventional muon and neutrino fluxes [1, 7, 8, 9] agree well with our results as shown in Fig. 10. The conventional muon flux from Gaisser [1] is shown as a dashed line in Fig. 10a as far in energy as it is applicable. Also shown as dashed lines in Fig. 10bc are the conventional neutrino fluxes from Volkova [7]. In contrast to these models, ours does not obey Feynman scaling. The scaling violations are apparent in Fig. 11a and from the deviation from a constant value of the production Z-moments (Fig. 4). Nevertheless, they are small enough that when folding everything together (initial spectrum, cascade interactions and decays) the resulting conventional muon and neutrino fluxes agree well with those models. We have thus confirmed previous results by an independent calculation based on a new approach using Monte Carlo simulations to more fully take into account the atmospheric cascade interactions producing secondary particles decaying into muons and neutrinos.

Concerning previous estimates of the flux of prompt muons and neutrinos, there are variations between different model calculations of up to a few orders of magnitude, as illustrated in Fig. 10. One should note that prompt fluxes are direction independent up to the charm particle critical energy $\sim 10^7$ GeV (Table 2) and therefore directly comparable independently of whether the horizontal or vertical direction has been considered in these estimates. Furthermore, due to the charmed particle decay kinematics and the same branching ratios for the semi-leptonic decays into electrons and muons, the prompt muon and neutrino fluxes are essentially the same (cf. the decay Z-factors in Table 3). Therefore, the curves for prompt muons in Fig. 10a are also taken

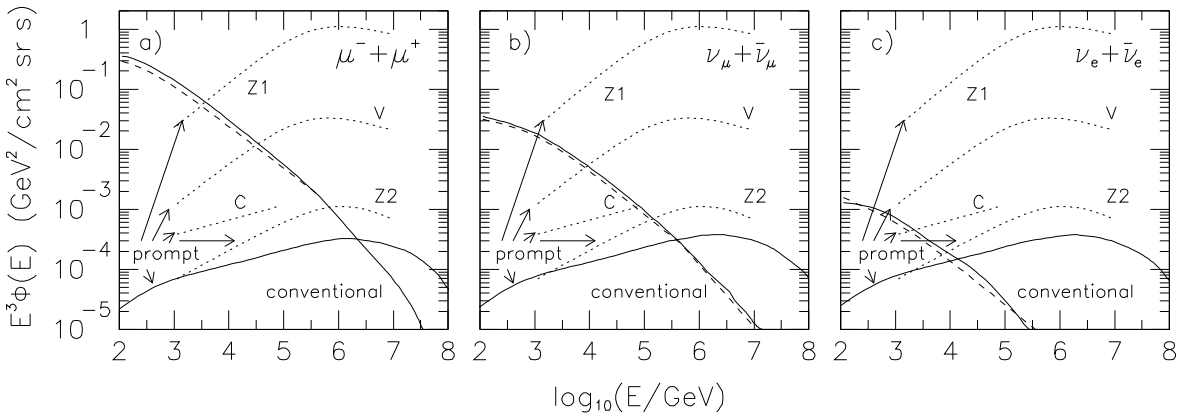

Figure 10: *Prompt and conventional muon and neutrino fluxes from our cascade simulation (solid curves) compared with earlier model calculations as discussed in the text.*

to represent the prompt neutrinos in Fig. 10bc (except for our own curves, which are calculated separately). The comparison in Fig. 10 shows that previous results are in general substantially larger than our results based on pQCD. Even the highest flux from our extreme version IC2 of the intrinsic charm hypothesis (Fig. 9) is lower than most previous calculations. These large differences are due to different models for charm production, both regarding the magnitude and the energy dependence of the cross section and the distribution in longitudinal momentum fraction x_F of the charmed particles.

The curves labeled V in Fig. 10 are from the calculation by Volkova *et al.* [17], applying the so-called 'quark-gluon string model' (QGSM) [70] (not to be confused with the Lund string model [32]). It uses a parametrised energy dependence of the charm cross section, curve labeled V in Fig. 7, normalized to early experimental data which are substantially above more recent measurements. The charm particle energy spectrum is assumed to obey Feynman scaling and has the form

$$dN/dx_F \sim (1-x_F)^\alpha \tag{46}$$

with $\alpha_D = 5$ and $\alpha_{\Lambda_c} = 0.4$ for D-mesons and Λ_c-baryons, respectively.

The curves marked Z1 in Fig. 10 are from Zas *et al.* [20] and illustrates an extreme model where the charm cross section is simply taken as 10% of the total inelastic cross section (cf. Fig. 7). This is substantially higher than all charm data as shown in Fig. 7. This model uses the scaling x_F-distribution of Eq. (46) with $\alpha_D = 3$ and $\alpha_{\Lambda_c} = 1$. Castagnoli *et al.* [15] obtained the result marked C in Fig. 10 using a parametrised energy dependent charm cross section shown by curve C in Fig. 7 based on some early data (band marked 11) that are higher than later measurements. Again, the differential spectra are of the form Eq. (46) using $\alpha_D = 5$ and $\alpha_{\Lambda_c} = 0.4$. The curves marked Z2, from Zas *et al.* [20], correspond to charm *quark* production calculated with leading order pQCD matrix elements using relatively hard parton distributions. This spectrum would be softened by taking hadronisation into account and thereby become even closer to our result, as expected since they are based on the same pQCD processes.

The first important difference between our model and previous ones lies in the magnitude and energy dependence of the charm production cross section. As demonstrated in Fig. 7 our

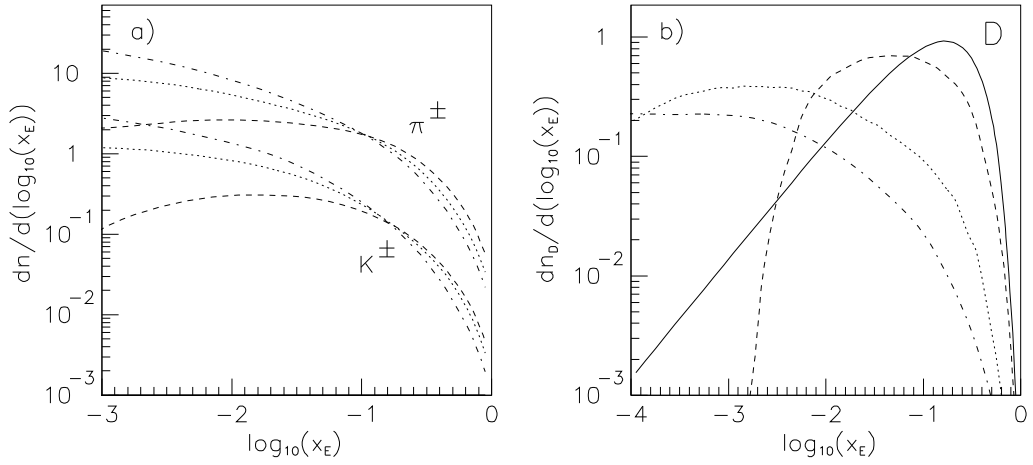

Figure 11: *Distribution in fractional energy x_E of produced mesons: (a) $\pi^{\pm}$ and $K^{\pm}$ mesons, (b) D mesons. Dashed, dotted and dashed-dotted lines are obtained from simulations with* PYTHIA *at proton beam energies of 10^3 GeV, 10^6 GeV and 10^9 GeV, respectively. The solid line represents Feynman scaling using Eq. (46) with $\alpha_D = 5$. (D-meson curves are normalized to unit area.)*

model reproduces available data on charm production cross sections, but the other models do not. In some cases one may have been mislead in the construction of the models by the early charm measurements that turned out to be substantially higher than the measurements done later.

Another important reason for our lower flux is the strong breaking of Feynman scaling as demonstrated in Fig. 11b. The x_F distributions for D-mesons produced at three different energies in our model are here compared with the energy-independent distribution in Eq. (46) with $\alpha_D = 5$. The Feynman scale breaking in our model arises in the perturbative charm quark production, but is also influenced by the hadronization model. As discussed in section 5.2, charm quark production is dominant close to threshold, $\hat{s} = x_1 x_2 s > 4m_c^2 c^4$. This effect does not disappear with increasing energy, but is rather enhanced with parton densities that increase at small x. This leads to a scale breaking with the charm quark x_F distribution in the symmetric nucleon-nucleon cms becoming softer around $x_F = 0$ with increasing cms energy. In the Lund hadronization model, the charm quark is connected by a colour string to a spectator parton. In the hadronization of this string, the produced charm hadron may obtain a larger longitudinal momentum than the charm quark, due to the momentum contribution from the parton with which it is joined. The string may even have so small invariant mass that it directly produces a charmed hadron, *i.e.* the charm quark effectively coalesces with a spectator parton into a charmed hadron. This latter process naturally happens particularly at small overall cms energies. Since these forward-'pulling' hadronization effects become less important with increasing collision energy, they also contribute to the Feynman scale breaking.

The effect on the prompt muon flux from this Feynman scale breaking is shown in Fig. 12. Our normal result is here compared with the results from a modification of our model, where in each event the charmed particles D and Λ_c are redistributed according to the scaling distribution in Eq. (46) with $\alpha_D = 5$ and $\alpha_{\Lambda_c} = 0.4$. Clearly, the Feynman scale breaking softens the spectrum considerably. (In comparing these curves one should note that there is no conserved integral of

the E^3-weighted flux.) To examine the effect of the energy dependence of the overall charm cross section, we have, in addition to using this scaling x_F-distribution, renormalized our simulated charm events to mimic the cross section in the model by Volkova *et al.* [17] mentioned above and shown by curve V in Fig. 7. Since this cross section is larger than in our model at energies below $\sim 10^6$ GeV and smaller above, this change flattens the muon spectrum in Fig. 12. With these two changes in the spirit of ref. [17], we obtain the same shape of the prompt muon flux as in [17] but with a lower overall normalization. The resulting spectra are, however, in reasonable agreement with the calculation of Castagnoli *et al.* [15] using a similar approach as ref. [17]. A more recent calculation based on the QGSM by Gonzalez-Garcia *et al.* [21] gives fluxes that are comparable to the fluxes predicted by Castagnoli *et al.* [15].

The calculation by Bugaev *et al.* [18] resulted in overall prompt fluxes slightly lower than in ref. [17]. They considered Feynman scaling violations in charm production through a phenomenological equation and obtained higher fluxes in the non-scaling case than in the scaling case, *i.e.* opposite to the effect we find and have just described. However, their way of introducing the energy dependence in the x_F distribution does not preserve the overall normalization, *i.e.* the integral of the x_F-distribution. This means that, in comparison with our model, there is not the same clear separation between the overall charm cross section normalization and the charm particle x_F distribution.

Since most of the earlier calculations are based on non-perturbative charm production mechanisms a comparison with our intrinsic charm model in section 6 is of interest, *i.e.* comparing Figs. 9 and 10. Intrinsic charm should be considered as a process in addition to the standard pQCD one, but the sum of their resulting fluxes is still lower than, *e.g.*, Volkova *et al.* [17]. To get a similarly high flux the rate of intrinsic charm must be increased substantially, about a factor 1000 for IC1 and 10 for IC2. Such rates are incompatible with the experimental limits on intrinsic charm and with measured inclusive charm cross sections (Fig. 7) and x_F-distributions.

This discussion has demonstrated significant effects on the high energy prompt muons and neutrinos depending on the assumptions made in the charm production model employed. The

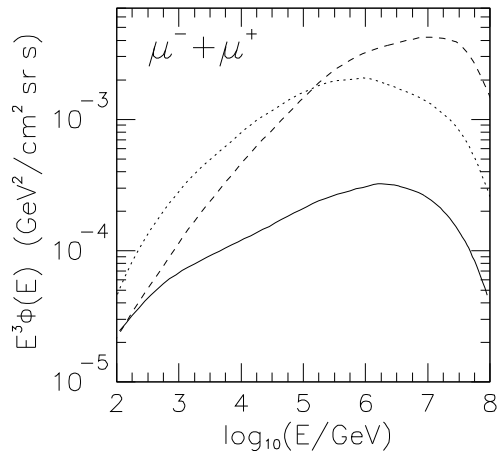

Figure 12: *The prompt muon flux in our model (solid line) and after re-distributing the generated charm particles to obey Feynman scaling using Eq. (46) (dashed line) and then also renormalizing the cross section to that of curve V in Fig. 7 from [17] (dotted curve).*

models in ref. [15, 17] give cross sections above more recent charm production data (Fig. 7) and apply simple Feynman scaling x_F-distributions. The model used by us, on the other hand, gives a fair description of measured charm production cross sections (Fig. 7) and applies well-motivated charm particle momentum distributions with significant Feynman scaling violations.

8 Conclusions and outlook

We have studied the production of neutrinos and muons in the atmosphere by collisions of cosmic rays with air nuclei, paying special attention to muons and neutrinos coming from decays of charmed particles (prompt fluxes). Two methods have been used to calculate the fluxes: a Monte Carlo simulation of the hadronic cascade in the atmosphere and an interpolation of asymptotic solutions to the transport equations. In both methods the PYTHIA Monte Carlo program has been used to simulate the primary collision and following cascade interactions. Results for the two methods are consistent. They agree with previous calculations of the conventional fluxes from decays of pions and kaons, but give substantially lower prompt components. This is due to different models for charm production, both regarding the energy dependence of the cross section and the longitudinal momentum distribution of the charmed particles. Whereas previous models give charm production cross sections above collected recent data and apply Feynman scaling for the longitudinal momentum distributions, our model gives a fair description of measured charm production cross sections and applies well-motivated charm particle momentum distributions with significant Feynman scaling violations. There is still some uncertainty (as discussed in section 5.2) when extrapolating this charm cross section calculation to the very high energies (10^9 GeV) needed for this study. Here, one cannot at present exclude a non-negligible contribution from some unconventional non-perturbative production mechanism. We investigate one such mechanism, namely that of intrinsic charm which has some theoretical motivation and some indications from data. This mechanism is likely to give a very small contribution to the total charm cross section, but the poorly known normalisation and energy dependence prevents a reliable prediction. Although disfavoured, a contribution $\sim 10\%$ of the pQCD charm cross section is presently not excluded, which through the harder momentum spectrum would lead to a dominant contribution of leptons at very high energies.

We find that prompt muons and muon-neutrinos overcome the conventional fluxes at an energy of 10^6 GeV, which is substantially higher than in some earlier estimates. According to our results, it will therefore be harder to use measurements of the prompt atmospheric fluxes to estimate the total charm production cross section at high energy. The situation is slightly different in the case of the electron-neutrinos, for which prompt fluxes dominate above 10^5 GeV. The electron-neutrino flux is, however, experimentally more difficult to measure and it is therefore a challenge to obtain the data needed to derive the charm production cross section.

On the positive side, the lower atmospheric neutrino fluxes we predict are a less severe background to measurements of neutrinos from astrophysical sources (for a review on these see [71]). To illustrate this, we show in Fig. 13 the vertical fluxes of conventional and prompt atmospheric muon-neutrinos calculated by us (solid lines) together with expected neutrino fluxes from such sources. Cosmic ray interactions with the interstellar medium produce neutrino fluxes through processes similar to the atmospheric case and we show results derived from [72] in the direction of the galactic center (dashed upper curve) and orthogonal to the galactic plane (dashed lower curve). Two estimates of diffuse neutrino fluxes from active galactic nuclei are also shown (dotted line from ref. [73] and dash-dotted line from ref. [74]). At high energies ($\gtrsim 10^5$ GeV), all of these fluxes are in excess of our predicted atmospheric neutrino background. This provides interesting prospects for large scale neutrino telescopes to detect high energy neutrinos from

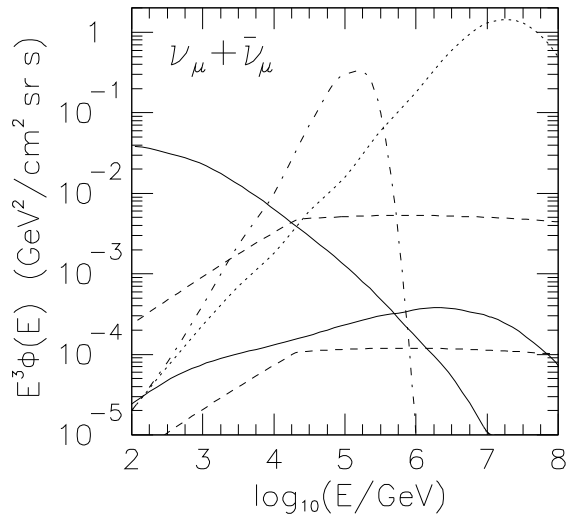

Figure 13: *Vertical fluxes of conventional and prompt atmospheric muon-neutrinos from our simulation (solid lines) compared to some astrophysical sources: the flux from cosmic ray interactions with the interstellar medium as derived from [72] (dashed upper curve: in the direction of the galactic center; dashed lower curve: orthogonal to the galactic plane) and the estimated diffuse fluxes from active galactic nuclei (dotted line [73], dash-dotted line [74]).*

cosmic sources.

Acknowledgements

We are grateful to T. Sjöstrand for useful discussions and to J. Rathsman for a critical reading of the manuscript. P. Gondolo wishes to thank the Uppsala and Stockholm Universities for support during his visits. This work has been partially funded by the Swedish Natural Science Research Council and the European Community through the Theoretical Astroparticle Network under contract No. CHRX-CT93-0120 (D.G. 12 COMA).

References

[1] T. K. Gaisser, *Cosmic Rays and Particle Physics* (Cambridge University Press, Cambridge, 1990).

[2] AMANDA Collaboration, in *23rd International Cosmic Ray Conference,* Calgary, Canada, July 1993, Vol.4, p.561.

[3] G. V. Domogatsky, in *TAUP 93,* ed. C. Arpesella, E. Bellotti and A. Bottino, Nucl. Phys. (Proc. Suppl.) **B35** (1994) 290.

[4] J. G. Learned, in *Neutrino 92,* ed. A Morales, Nucl. Phys. (Proc. Suppl.) **B31** (1993) 456.

[5] L. K. Resvanis, in *TAUP 93,* ed. C. Arpesella, E. Bellotti and A. Bottino, Nucl. Phys. (Proc. Suppl.) **B35** (1994) 294.

[6] M. Thunman, Licentiate thesis, Uppsala University, TSL/ISV-94-0097.

[7] L. V. Volkova, Yad. Fiz. **31** (1980) 1510 [Sov. J. Nucl. Phys. **31** (1980) 784].

[8] T. K. Gaisser, T. Stanev and G. Barr, Phys. Rev. **D38** (1988) 85; G. Barr, T. K. Gaisser and T. Stanev, Phys. Rev. **D39** (1989) 3532.

[9] P. Lipari, Astropart. Phys. **1** (1993) 195.

[10] For a review of the 1993 status, see E.V. Bugaev *et al.*, *Proceedings of the 3rd NESTOR International Workshop*, Pylos (Greece), 1993, ed. L.K. Resvanis, p. 268.

[11] W. Rhode, *TAUP93*, Gran Sasso (Italy), 1993, ed. C. Arpesella, E. Bellotti and A. Bottino, Nucl. Phys. B (Proc. Suppl.) 35 (1994) 250.

[12] M. Ambrosio *et al.* (MACRO Collaboration), Phys. Rev. **D52** (1995) 3793.

[13] M. Aglietta *et al.* (LVD Collaboration), Astropart. Phys. **3** (1995) 311.

[14] L.V. Volkova and G. T. Zatzepin, Yad. Fiz. **37** (1983) 353 [Sov. J. Nucl. Phys. **37** (1983) 212].

[15] C. Castagnoli *et al.*, Nuovo Cimento **A82** (1984) 78.

[16] H. Inazawa, K. Kobayakawa and T. Kitamura, Nuovo Cimento **C9** (1986) 382.

[17] L.V. Volkova, W. Fulgione, P. Galeotti and O. Saavedra, Nuovo Cimento **C10** (1987) 465.

[18] E.V. Bugaev, E.S. Zaslavskaya, V.A. Naumov and S.I. Sinegovsky, in *20th Int. Cosmic Ray Conference,* Moscow 1987, Vol. 6, p. 305.

[19] E.V. Bugaev, V.A. Naumov, S.I. Sinegovsky and E.S. Zaslavskaya, Izv. Akad. Nauk SSSR, Ser. Fiz. **53** (1989) 342 [Bull. Acad. of Sci. of the USSR, Phys. Ser. **53** (1989) 135].

[20] E. Zas, F. Halzen and R.A. Vázques, Astropart. Phys. **1** (1993) 297.

[21] M. C. Gonzalez-Garcia, F. Halzen, R.A. Vázques and E. Zas, Phys. Rev. **D49** (1994) 2310.

[22] P. Pal and D. P. Bhattacharyya, Nuovo Cimento **C15** (1992) 401.

[23] T.H. Burnett *et al.*, *Proceedings of the XXI International Cosmic Ray Conference, Adelaide, 1990*, Vol. 3, p. 101.

[24] S. Ahlen *et al.*, Phys. Rev. **D46** (1992) 895.

[25] M. Honda, T. Kajita, K. Kasahara and S. Midorikawa, *Calculation of the Flux of Atmospheric Neutrinos*, ICR-Report-336-95-2.

[26] A. Gregory and R. W. Clay, in *CRC Handbook of Chemistry and Physics* (CRC Press Inc., Boca Raton, Florida, 1982–1983) p. F-175.

[27] C. W. Allen, *Astrophysical Quantities* (The Athlone Press, London, 1983).

[28] J. Ashman *et al.*, Z. Physik **C52** (1991) 1 and references therein.

[29] J. Shukraft *et al.*, HELIOS Collaboration, Nucl. Phys. **A498** (1989) 79c.

[30] T. F. Hoang, Z. Phys. **C61** (1994) 341.

[31] T. Sjöstrand, PYTHIA 5.7 & JETSET 7.4, Comput. Phys. Commun. **82** (1994) 74

[32] B. Andersson, G. Gustafson, G. Ingelman and T. Sjöstrand, Phys. Rep. **97** (1983) 33.

[33] Particle Data Group, Phys. Rev. **D50** (1994) 1.

[34] W. R. Frazer *et al.*, Phys. Rev. **D5** (1972) 1653.

[35] Z. Garraffo, A. Pignotti and G. Zgrablich, Nucl. Phys. **B53** (1973) 419.

[36] A. Martin, R. Roberts and J. Stirling, Phys. Lett. **B354** (1995) 155.

[37] P. Nason, S. Dawson and R.K. Ellis, Nucl. Phys. **B327** (1989) 49; *ibid.* **B335** (1990) 260.

[38] M.L. Mangano, P. Nason and G. Ridolfi, Nucl. Phys. **B373** (1992) 295.

[39] L. Cifarelli, E. Eşkut and Yu.M. Shabelski, Nuovo Cimento **A106** (1993) 389.

[40] H1 Collaboration: I. Abt *et al.*, Nucl. Phys. **B407** (1993) 515; T. Ahmed *et al.*, .Nucl. Phys. **B439** (1995) 471.

[41] ZEUS Collaboration: M. Derrick *et al.*, Phys. Lett. **B316** (1993) 412; Z. Phys. **C65** (1995) 379, Phys. Lett. **B345** (1995) 576.

[42] A. Martin, R. Roberts and J. Stirling, Phys. Lett. **B306** (1993) 145.

[43] G.A. Schuler and T. Sjöstrand, Nucl. Phys. **B407** (1993) 539.

[44] P. E. Karchin, E769 Collaboration, *Current Issues in Open Charm Hadroproduction and New Preliminary Results from Fermilab E769*, FERMILAB-Conf-95/053-E.

[45] M. Aguilar-Benitez *et al.*, Phys. Lett. **B189** (1987) 476.

[46] M. Jonker *et al.*, Phys. Lett. **96B** (1980) 435.

[47] M. E. Duffy *et al.*, Phys. Rev. Lett. **57** (1986) 1522.

[48] P. Fritze *et al.*, Phys. Lett. **96B** (1980) 427.

[49] R. Ammar *et al.*, Phys. Rev. Lett. **61** (1988) 2185.

[50] K. Kodama *et al.*, Phys. Lett. **263B** (1991) 573.

[51] M. J. Leitch *et al.*, Phys. Rev. Lett. **72** (1994) 2542.

[52] A. G. Clark *et al.*, Phys. Lett. **77B** (1978) 339.

[53] P. Chauvat *et al.*, Phys. Lett. **B199** (1987) 304.

[54] M. Basile *et al.*, Nuovo Cimento **67A** (1982) 40.

[55] A. Contin *et al.*, in *Int. Conf. on High Energy Physics,* Lisbon 1981, eds. J. Dias de Deus and J. Soffer, p. 835.

[56] G. Bari *et al.*, Nuovo Cimento **104A** (1991) 571.

[57] O. Botner *et al.*, Phys. Lett. **B236** (1990) 488.

[58] A. Alves *et al.*, Phys. Rev. Lett. **70** (1993) 722.

[59] M. Adamovich *et al.*, Phys. Lett. **284B** (1992) 453.

[60] S.J. Brodsky, P. Hoyer, C. Peterson and N. Sakai, Phys. Lett. **B93** (1980) 451.
S.J. Brodsky, C. Peterson and N. Sakai, Phys. Rev. **D23** (1981) 2745.

[61] S.J. Brodsky *et al.*, Nucl. Phys. **B369** (1992) 519.

[62] R. Vogt, S.J. Brodsky and P. Hoyer, Nucl. Phys. **B360** (1991) 67.

[63] R. Vogt, S.J. Brodsky and P. Hoyer, Nucl. Phys. **B383** (1992) 643.

[64] E. Hoffman and R. Moore, Z. Phys. **C20** (1983) 71.

[65] B.W. Harris, J. Smith and R. Vogt, *Reanalysis of the EMC Charm Production Data with Extrinsic and Intrinsic Charm at NLO*, FSU-HEP-951030, ITP-SB-95-15, LBL-37266.

[66] R. Vogt and S.J. Brodsky, Phys. Lett. **B349** (1995) 569.

[67] R. Vogt and S.J. Brodsky, *Charmed Hadron Asymmetries in the Intrinsic Charm Coalescence Model*, SLAC-PUB-95-7068, LBL-37666.

[68] G. Ingelman and M. Thunman, in preparation.

[69] M. S. Kowitt *et al.*, Phys. Rev. Lett. **72** (1994) 1318.

[70] A.B. Kaidalov and O.I. Piskunova, Z. Physik **C30** (1986) 145

[71] V.S. Berezinsky, S.V. Bulanov, V.A. Dogiel and V.S. Ptuskin, *Astrophysics of Cosmic Rays* (North Holland, Amsterdam, 1990).

[72] G. Domokos, B. Elliott and S. Kovesi-Domokos, J. Phys. **G19** (1993) 899.

[73] A. P. Szabo and R. J. Protheroe, in *Proc. Workshop on High Energy Neutrino Astrophysics,* Honolulu, eds. V. J. Stenger *et al.* (World Scientific, Singapore, 1992) p. 24.

[74] M. Sikora and M. Begelman, in *Proc. Workshop on High Energy Neutrino Astrophysics,* Honolulu, eds. V. J. Stenger *et al.* (World Scientific, Singapore, 1992) p. 114.